Doctoral Dissertation (Censored)

博士論文 (要約)

Characterization of the EUV Hydrogen Lyman Transitions in the Solar Atmosphere

(太陽大気における極紫外水素ライマン線の

特徴に関する研究)

A Dissertation Submitted for the Degree of Doctor of Philosophy

May 2021

令和 3 年 5 月 博士 (理学) 申請

Department of Earth and Planetary Science,

Graduate School of Science, The University of Tokyo

東京大学大学院理学系研究科地球惑星科学専攻

Takahiro Hasegawa

長谷川 隆祥

Abstract

The Sun's outer atmosphere (corona) is much hotter at several million K than its surface (photosphere) that only reaches $\sim$ 6,000 K. The reason why the outer atmosphere has a higher temperature than the lower part that is closer to core, i.e., energy source of the star, is one of the most important mysteries in the astrophysics and is defined as the "coronal heating" problem. To produce and maintain the corona, we need mechanisms to non-thermally transport the photospheric turbulent energy to the upper atmosphere in some forms without dissipations, and then, to convert them into the heat.

To solve the mystery, it is essential to understand the physics and plasma conditions in the chromosphere, the interface atmosphere of the energy source and the region where the energy is converted into the heat, i.e., the photosphere and the corona. This is because the chromosphere is also heated by non-thermal energy transport and dissipation, and is full of dynamic phenomena which have a role on heating the corona, such as jets and magnetic reconnection. However, the intermediate plasma conditions in the chromosphere make complicated an accurate realistic modeling of its dynamics and the radiative transfer, thus interpreting the observations of chromospheric emission. Hence, our access to the chromospheric spectral lines is limited. For a better understanding of the atmospheric heating, we have to access new spectral windows that fill the diagnostic gaps in the chromosphere.

In this dissertation, we suggest that the hydrogen Lyman transitions, which fall in the extreme ultraviolet (EUV) regime, are good candidates for the purpose. On the other hand, our knowledge on the spectroscopic and formation properties of the Lyman lines

is far from satisfactory because of limited observations of the lines and difficulties on modeling the chromospheric spectral lines.

Motivated by the situation mentioned above, we focus this dissertation on characterizing the spectral features of the Lyman lines, in particular Lyβ, by solving the full non-local thermal equilibrium (NLTE) radiative transfer considering the partial redistribution (PRD) effects and numerically modeling the Lyman spectra. We relate the response of its core, wing, and spectral shape to the atmospheric properties in the chromosphere and reveal how the Lyβ bridges the diagnostic gaps and how the line contributes to solving the coronal heating problem.

In Chapter 2, we firstly synthesized Lyβ spectra emerging from the 3D realistic simulated atmosphere (Gudiksen et al., 2011; Carlsson et al., 2016). We found that the core forms in the upper chromosphere of T $\sim$ 23,000 K. The Doppler shifts found for the line core correspond to the vertical velocity at the formation height in the model atmosphere, and the core intensities are well correlated to the squared electron density and the solar features' geometry there. We concluded that the Lyβ core is an excellent diagnostic to probe the upper chromosphere.

We also computed the response function to some physical parameters with the 1D FAL-C atmospheric model (Fontenla et al., 1993) and found the wing's response to temperature perturbations in 1.1-2.1 Mm and to the line-of-sight (LOS) velocity perturbation in 1.7-2.1 Mm, respectively. Thus, the Lyβ wing is sensitive to lower atmospheric layers in the middle to upper chromosphere. In Chapter 3, we took a step further, aiming to understand the relation between the Lyβ spectral features, e.g., line asymmetries, and the atmospheric properties, e.g. temperature or LOS velocity, in the 3D realistic simulation. We applied a cluster analysis on the synthesized Lyβ spectra based only on the shape of the profile, which allowed us to determine 32 groups. We derived the relation between a typical spectral profile and the corresponding typical stratifications of the atmospheric parameters in each group. We discovered that we could narrow down the obtained 32 groups to six families of profiles that shared similar spectral features. This extra grouping

helped us define the relationship between spectral shapes and atmospheric structures, as follows:

1. Regarding the temperature structure, a single peak Lyβ emerges from a narrower chromosphere having a transition region (TR) with a drastic temperature increase at low height. In contrast, Lyβ with central reversal originates from a broad and upward-extended chromosphere with a smooth temperature increase in a TR.

2. Regarding LOS velocity structure, these are two types of families of self-reversed Lyβ. A Lyβ spectrum having a strong emission peak at shorter wavelengths (i.e., blue peak) than that at longer wavelengths (i.e., red peak) originates from a positive velocity gradient in the middle to upper chromosphere. In contrast, a stronger red peak corresponds to a negative velocity gradient there. We statistically discovered a correlation between the peak asymmetries and the velocity gradients.

3. A small fraction of synthesized spectra has a bright emission at their wing and continua, caused by temperature enhancements at lower atmospheric layers, just above the temperature minimum. Converging flows may heat up the plasma in the lower atmosphere.

The spatial distribution of the six families on the magnetic loop structure in the 3D model atmosphere reveals that the Lyβ with deep core reversal (and a stronger red peak) corresponds to the loop top where the LOS is perpendicular to the magnetic field.

In Chapter 4, we further applied the cluster analysis on observations of Lyβ spectra taken by the *Solar Ultraviolet Measurements of Emitted Radiation* (SUMER, Wilhelm et al., 1995; Lemaire et al., 1997) instrument on board the *Solar and Heliospheric Observatory* (SoHO, Domingo et al., 1995) spacecraft. We discovered that deeply reversed Lyβ spectra tend to be distributed at the boundary of magnetic field concentrations, in particular, between positive and negative magnetic patches, which is consistent with that found in the synthesized spectra. We detected some discrepancies between synthesized

and observed spectra, though. For example, the spectra with bright continuum emissions found in the synthesized spectra are not detected in the observations.

Furthermore, we added Lyα spectra to our analysis in Chapter 5. We studied the relationship between the Lyα and β peak asymmetries and the structure of the LOS velocity. We found that the peak asymmetry relation is associated with the height where the downflow peak is located. Regarding their asymmetries, previous observations revealed that the combination of Lyα with a stronger blue peak and Lyβ with a larger red peak is preferred in the disk center quiet Sun. Our findings on the asymmetries will be helpful to deduce the chromospheric velocity structure accurately.

Previous observations revealed a pervasive downflow in the upper-chromosphere and the TR, and an upflows in the lower corona. The Lyβ asymmetry is related to the trend in the vertical velocity stratification. However, the structures derived by realistic MHD simulations or by Doppler shift analysis of multiple EUV lines are not consistent with the red-asymmetry preference of Lyβ, and more detailed spectroscopic observations resolving the chromosphere are required (Chapter 6).

In conclusion, these studies revealed the Lyman lines potentially fill the chromospheric diagnostic gaps and help us understand the physical properties there, which has a crucial role in heating the upper atmosphere. In future observations, the strong emission of Lyman lines will enable high cadence spectroscopic observations, and with them, the identification of the wave modes and estimation of the energy flux of high-frequency MHD waves. For tall protruding structures, such as spicules, the diagnostic gaps are more significant, and an observation with multiple chromospheric lines, including the Lyman transitions, will be a powerful tool to detect waves propagating through them, and to trace the heating process at its upper edge. Our new diagnostic capability, i.e., the peak asymmetry of Lyβ, can be applied to quantify an acceleration at the root of a spicule, which will allow us to distinguish its formation process. Space-born EUV spectrometers will achieve these proposed observations in the next generation of the 2020's, i.e., the *Solar-C (EUVST)* and *Solar Orbiter*/SPICE, and our achievements in this dissertation will be

theoretical rationales to interpret the Lyman spectra taken in the future observations.

Acknowledgments

I would like to show my sincere gratitude to my supervisor, Dr. Toshifumi Shimizu. His insightful and patient guidance allows me to reach the goal of this long road for the Ph.D. I learned a lot of things from his supervision. I also show my kind appreciation to Dr. Carlos Quintero Noda, who gave me an opportunity to start this interesting and important project. He encouraged me to conquer obstacles in my resaerch activities, sometimes as a mentor, at other times, as a friend. I am deeply grateful of Dr. Luca Teriaca, who is a host researcher of my one-week visit to the Max-Planck Institute for Solar System Research to learn how to use the SUMER data archive, and even after the visit he answered my questions. I greatly thank to Dr. Mats Carlsson for his instructive advice to our research. I appreciate the valuable discussions with Dr. Takaaki Yokoyama, which help me improve this dissertation. I have been tremendously supported by my office mates; Y. Bamba, S. Ishikawa, T. Kawate, T. Matsumoto, T. Oba, T. J. Okamoto, A. Tei, S. Toriumi, Y. Kawabata, T. Doi, M. Abe, R. Tani, M. Koyama, M. Yoshida, I. Yamagishi, K. Daiguji, K. Matsuzaki, T. Sakao, and D. Brooks. Without them, I could not finish this tough journey. Finally, I want to express my great thanks to the supports from my family.

Contents

Chapter 1

Introduction

The Sun is a unique star we can observe its atmospheric structures from the earth with high spatial resolution. The knowledge on the Sun can be extended to the other stars we cannot spatially resolve. Understanding the Sun is also essential for the heliosphere because plasma and magnetic field leaking from the Sun reach the planets in the solar system, governing the environment of their atmospheres. Furthermore, activities in the Sun have significant impacts on the lives of humanity on the earth. Radiations and plasma ejections originating from energetic activities, e.g., solar flares and coronal mass ejections, can leave unrecoverable damages on human's society. For these reasons, comprehensive knowledge of the Sun leads to understanding the origin, present, and future of our lives.

1.1   Solar Atmosphere

The temperature and mass density stratification shown in Fig. 1.1 indicates that the Sun has a stratified and highly structured outer atmosphere composed of three regions, i.e., photosphere, chromosphere, and corona. In addition, due to a drastic temperature increase, the region between the chromosphere and corona is called transition region (TR). Each region is characterized by significantly different plasma conditions, and the formation of such atmospheric structure is one of the most fascinating mysteries in solar physics.
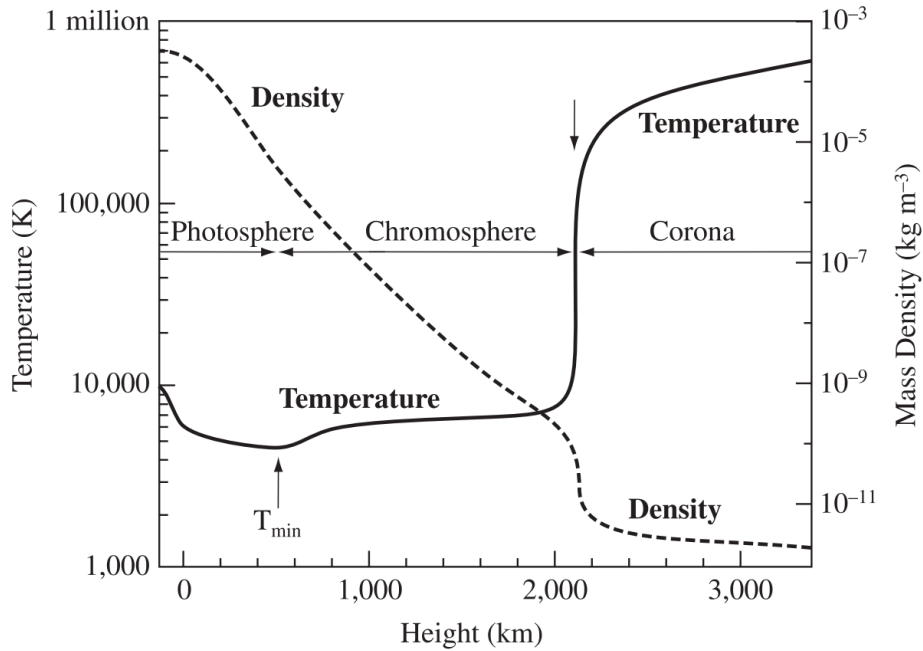
Figure 1.1: The model of the height dependence of thermal parameters. The vertical arrow between the chromosphere and corona indicates that the drastic temperature increase corresponds to the transition region. The figure is reprinted from Priest (2014).

Photosphere

The Sun's surface is defined as the thin layer where the optical depth of the atmosphere is unity. Exactly speaking, the height where the optical depth equals unity at 500 nm continuum, where the temperature and mass density is $\sim 6,600$ K and $\sim 10^{23}$ m^{-3}, respectively, is defined 0 km in geometric height (Priest, 2014). The temperature decreases with height to $\sim 4,400$ K at ~ 500 km height, i.e., temperature minimum (Priest, 2014). The thin region from the optical surface at 500 nm to the temperature minimum is often called "photosphere".

Inside the Sun, nuclear fusion takes place in the core, and the energy is thermally transported outward to the surface, i.e., by radiation from the core to 0.7 solar radius (radiative zone) and by convection from 0.7 solar radius to near the photosphere (convection zone). Gases lifted by the convection cool down at the photosphere mainly by radiation, resulting in denser gases that fall back to the surface. These fountain-like flows form the

2

cellular patterns filling out the photosphere, called granules, each of which has a size in order of 1,000 km. There is a less apparent convective pattern larger than a granule, i.e., a super granule, with the cell size of 30,000 km. The convective flow sweeps the magnetic field to the boundary of super granular cells, and the magnetic concentration forms the large-scale network structure through the solar atmosphere (Wedemeyer-Böhm et al., 2009).

Due to the large density at the photosphere, the ratio of plasma to magnetic pressure, i.e., the plasma β, is greater than unity in general, except for active regions (such as sunspots or pores) where the magnetic field is stronger (Gary, 2001). The plasma β is defined as

$$\beta = \frac{2\mu_0 p}{B^2} \tag{1.1}$$

with μ_0 the vacuum permeability, p the gas pressure, and B the magnetic field. Thus, in the cases where $\beta > 1$, the plasma dynamics is dominated by the gas motion.

Chromosphere

Starting from the temperature minimum, we have a temperature increase to $\sim 10^4$ K in a thin region, i.e., the chromosphere. The plasma conditions are intermediate, with the temperature of $\sim 10^4$ K and the density of $\sim 10^{19}$ m^{-3} (Priest, 2014), resulting in the complicated physics in the chromosphere. In many cases, plasma β becomes unity at some point in the chromosphere (Gary, 2001). Therefore, we have a transition from high to low β plasma. The plasma is partially-ionized, thus ambipolar diffusion takes place.

Chromosphere typically extends to 2,000 km height (see Fig. 1.1). However, in some part, thread-like protrusions called spicules (Beckers, 1968, 1972) reach the coronal height. It has been understood that the chromosphere is a very dynamic region constituted of a collection of innumerable spicules (De Pontieu et al., 2007a). Furthermore, spicules are key elements to understanding the atmospheric heating (De Pontieu et al., 2009).

When the quiet Sun chromosphere is observed in the extreme ultra violet (EUV), the network structure constructs the super granular pattern. This is formed by magnetic flux swept to the boundary of super granules, and bright network regions correspond to strong patchy magnetic flux (Reeves, 1976).

Transition Region

Just above the chromosphere, the temperature drastically rises to $\sim 10^6$ K in narrow height scale of ~ 200 km. This thin layer with the extreme temperature gradient is named "transition region (TR)". The drastic rise of temperature happens because the hydrogen is fully ionized, and the energy can be used to increase temperature. Heat conduction from the corona effectively works due to large temperature gradient, and the energy flow is balanced by radiative energy loss (Fontenla et al., 1990). Therefore, the TR is essential for the energy balance in the Sun's atmosphere (Fontenla et al., 1990, 1991, 1993).

Corona

Above the TR, a very hot and tenuous atmosphere, i.e., "corona", extends. In the corona, the temperature reaches several MK. The typical density at the inner corona is $\sim 10^{14}$ m^{-3} (Priest, 2014). Due to its extremely low density, the plasma β is lower than unity, and the magnetic field dominates the plasma dynamics.

Coronal features can be separated into two types: open or closed magnetic field. A coronal hole (Cranmer, 2009) is observed as a dark area in the EUV and soft X-ray coronal observations. This region is mostly occupied by the open magnetic field outgoing to the interplanetary space. The particle density is tenuous, and emission is faint. The mass in the corona is carried outwards by solar winds (Zirker, 1977). Closed magnetic loops appear in some forms in the X-ray or EUV observations. Coronal loops (Reale, 2014) represent the magnetic flux bundles filled with hot plasma. On the smaller side, coronal bright points (Madjarska, 2019) are observed at the locations where small bipolar magnetic fluxes are observed on the photosphere.

The height variation of temperature (Fig. 1.1), in which the outer atmosphere (corona) is hotter than inner (photosphere) with the energy source at the core, cannot be explained by the thermal energy transportation (e.g., thermal conduction, radiation, and convection). Therefore, the non-thermal mechanisms to transport the energy from the photosphere to the corona and convert it to the heat are required to produce and maintain the hot corona. Although many authors have dedicated their efforts to solving the mystery of this "coronal heating" problem, this is still open due to the difficulty in the observations of the energy dissipations in the tenuous corona and lack of quantitative estimation on energy flux injected in the corona. In the next section, we will give a brief review on the atmospheric heating with the emphasis on the importance of the plasma diagnostics in the chromosphere.

1.2 Atmospheric Heating

1.2.1 General Description

The photospheric convective energy is the primary candidate of the energy source to heat the upper atmosphere. The energy flux of $\sim 10^4$ and $\sim 10^3$ W m^{-2} are required to maintain the hot chromosphere and corona, respectively (Athay, 1976; Withbroe & Noyes, 1977; Anderson & Athay, 1989b). Despite the much hotter temperature in the corona, ten times larger energy flux is required to heat the dense chromosphere. The turbulent convective energy can be estimated as $\rho \langle \delta v^2 \rangle \langle \delta v \rangle = 10^5$ W m^{-2} where turbulent velocity and density in the photosphere are assumed ~ 1 km s^{-1} and ~ 0.1 g m^{-3}, respectively, and is sufficient to heat the upper atmosphere. Therefore, it is crucial to identify the process of transporting a part of the photospheric convective energy upward without being thermalized and dissipating in the corona, among a variety of heating phenomena (Klimchuk, 2006). Magnetic field is considered to take a key role in the heating, and we have three major hypotheses: (1) nano-flare heating, (2) wave dissipation, and (3) mass and energy

supply with spicules.

A solar flare is the most significant explosive event to convert magnetic energy to thermal energy via magnetic reconnection (Shibata & Magara, 2011). However, the frequency distribution of solar flares of 10^{27-32} erg indicates that the intermediate and large flare cannot supply the energy to keep the hot corona (Shimizu, 1995). Therefore, to maintain the several MK corona with the energy deposition by small-scale flares, that is, nano-flares with the energy less than 10^{26} erg, which cannot be sufficiently resolved and observed by the current facilities, have to occur much more frequently than larger flares (Hannah et al., 2011). Plausible mechanisms to cause frequent occurrences of nano-flares is the relaxation of magnetic stress in the braided magnetic flux generated by photospheric shuffling motions (Parker, 1972, 1983, 1988). Magnetic stress forms small-scale current sheets, which may be immediately dissipated by magnetic reconnection, giving the energy to the corona. In this sense, we have to derive the frequency distribution of nano-flares smaller than 10^{26} erg by detecting such small and faint events.

The photospheric convection generates upward-propagating waves in a variety of forms. The compressible longitudinal acoustic wave is excited in the photosphere. Still, such waves cannot transport the convective energy to higher than the chromosphere because the acoustic wave is subject to steepening due to the drastic change in thermal conditions and gravitational damping. On the other hand, an incompressible transverse wave propagating along magnetic field, i.e., the Alfvén wave, is less affected by the steepening and can transport the energy to a higher height. The energy carried by the Alfvén wave can heat the upper atmosphere if dissipated. However, the dissipation process of the Alfvén wave is under debate, with resonance absorption (e.g., Ionson, 1978) and phase mixing (e.g., Heyvaerts & Priest, 1983) as plausible mechanisms.

Spicules are presented as a reasonable mechanism to supply mass and energy from the chromosphere to the corona. Two types of spicule phenomena are determined; classical type-I spicules are of a long duration of ~ 10 min with slow speeds of $\sim$ 20-30 km s^{-1} (Beckers, 1968), whereas type-II spicules are dynamic jet-like phenomena of a short du-

ration of $\sim$ 10-100 s with fast speeds $\sim$ 50-150 km s^{-1} (De Pontieu et al., 2007a). While type-I spicules seem to be produced by magneto-acoustic shocks (Hansteen et al., 2006), the generation of type-II spicules may be associated with magnetic reconnection (De Pontieu et al., 2007b; Langangen et al., 2008; Samanta et al., 2019). The mass of spicules is $\sim$ 100 times larger than that of solar wind (Pneuman & Kopp, 1978). Therefore, a small fraction of the chromospheric plasma ejected upward can compensate the mass loss in the corona.

The interrelationship of these three mechanisms makes the atmospheric heating problem further challenging. For instance, magneto-acoustic waves excited in the photosphere cannot propagate to the upper atmosphere, but magnetic reconnection generates magneto-acoustic waves at the height, and their dissipation can heat the corona (Sturrock et al., 1999; Klimchuk, 2006). As well, spicules work as guides of MHD waves to the upper atmosphere. Low-frequency oscillations were observed along with spicules which have sufficient energy to heat the corona (De Pontieu et al., 2007b; McIntosh et al., 2011).

1.2.2 The Role of the Chromosphere on the Atmospheric Heating

These days the chromosphere is one of the areas where a lot of scientists have been paying attention to on solving the coronal heating problem because of the following two aspects.

First of all, the chromosphere is where non-thermal heating takes place tremendously. As stated in the previous section, to maintain the temperature of the chromosphere in a few ten kK, we need an energy flux ten times larger than that required for maintaining the temperature of the corona. The Alfvén wave and nano-flares are considered to be plausible mechanisms. Also, slow-mode acoustic waves excited by the photospheric turbulence are important to heat the lower chromosphere because most of the acoustic waves dissipate, develop the shocks, and convert their energy to the heat at the height (Anderson & Athay, 1989a). The hydro-dynamic model by Carlsson & Stein (1997) reproduced the chromospheric Ca II H emission enhanced by acoustic shocks. On the other hand, the acoustic

waves may not reach the upper chromosphere because they dissipate before reaching the height (Anderson & Athay, 1989a). Therefore, the same as heating the corona, we need some mechanisms to transport the energy to the upper chromosphere without dissipation. One possibility is mode conversion of fast magnetoacoustic waves into incompressible Alfvén waves at the height where the Alfvén velocity is equivalent to the sound speed (Cally & Goossens, 2008). The converted Alfvén waves may be important for heating the upper chromosphere (Grant et al., 2018).

Secondly, the chromosphere is the interface between the energy source (i.e. photo-sphere) and the heated region (i.e., corona), therefore it is the media transporting the energy to the outer atmosphere. Magnetic reconnection occurring in the chromosphere may play an essential role in heating the upper atmosphere. Hansteen et al. (2010) implemented in their 3D realistic simulation the episodic injection of emerging mag-netic flux into the upper chromosphere which reconnects with the pre-existing field and forms the hot upper atmosphere. They suggested that the localized heating in the upper-chromosphere, TR, and lower corona naturally results in red shifts in the TR and blue shifts in the low corona, which have been determined from Doppler shifts of a plenty of spectral lines (Doschek et al., 1976; Peter & Judge, 1999; Teriaca et al., 1999; Dadashi et al., 2011) and are considered as a constraint in modeling the atmospheric heating.

Such reconnection events may also be important to accelerate chromospheric jets, i.e., spicules, which are considered to have a role on energizing the upper atmosphere (De Pontieu et al., 2009). Emission enhancements in the blue wing of coronal EUV lines have been observed at footpoints of disk center active region loops, resulting in the line asymmetry (Hara et al., 2008). Such an asymmetry does not determined in the limb obser-vations. This asymmetry may be due to the second blue-shifted component at magnetic loop footpoints, implying that type-II spicules of chromospheric temperature are accel-erated and heated to the coronal temperature (De Pontieu et al., 2009; McIntosh & De Pontieu, 2009; De Pontieu et al., 2011; McIntosh et al., 2012). Similar blue-shifted fea-tures have been identified in the cooler Ca II 854.2 nm and Hα chromospheric spectral

lines as rapid blue-shifted excursions (RBEs) in the coronal hole boundary (Rouppe van der Voort et al., 2009). On the other hand, the formation mechanism of spicules, i.e., the shock heating or magnetic reconnections, is still under debate. For further understanding spicule's role on the atmospheric heating, it is required to determine its acceleration mechanism quantitatively.

Incompressible waves are attractive candidates to transport the energy from the photosphere without dissipation and heat the corona, and direct detections of such waves have been achieved in morphology of some chromospheric temperature structures as spicules (De Pontieu et al., 2007b) and prominences (Okamoto et al., 2007). De Pontieu et al. (2007b) interpreted the detected waves as Alfvén waves and derived the energy flux of 4-7,000 W m^{-2}. However, when these waves are assumed to be kink waves, the energy flux is modified to be 2-700 W m^{-2} (Van Doorsselaere et al., 2014). Recently, the direct detection of a torsional Alfvén wave was achieved for an active region filament (Kohutova et al., 2020). The detection of wave mode and direct measurements of the energy flux by such waves are quite important to identify the mechanisms responsible for the heating of the corona. However, since the incompressible waves do not cause intensity disturbance, detection of the waves are difficult tasks, and high spatial and temporal spectroscopic observations are required to identify line-of-sight (LOS) velocity oscillations or sinusoidal pattern in the morphology.

1.2.3 Chromospheric Diagnostic

The chromosphere is full of the dynamic phenomena relevant to the atmospheric heating. Hence, detailed observations of the chromosphere play a great role on revealing the heating mechanism. In probing the solar plasma properties from distant, i.e., from the earth, solar radiation measurements with remote sensing techniques have been almost one and the only way to have access to the chromosphere. To derive as much information as possible from the radiation, spectroscopic observations of spectral lines have made a significant

contribution to our scientific activities.

A bound-bound transition of an electron emits (or absorbs) light of a wavelength corresponding to the difference between two relevant atomic energy states. In the emission spectrum, this feature is found as brighter (or fainter) emergent intensity and called a "spectral line" or just a "line". A spectral line is characterized by a discrete and fixed wavelength. However, an emitted spectral line has broad wings, due to Gaussian-like absorption profile broadened by various mechanisms, e.g., Doppler broadening due to thermal motions, collisional broadening, and natural broadening due to the uncertainty principle. Therefore, while the line core has larger opacity and its formation height is higher than the other part of the line, line wings form at lower heights.

The formation of spectral lines emanated from the photosphere and corona is relatively simple. However, intermediate plasma conditions in the chromosphere make the modeling and interpretation of the chromospheric lines quite difficult (Carlsson et al., 2019). In the chromosphere, we have a transition from Local Thermal Equilibrium (LTE) where the radiation field is determined by a local thermal condition, to Non-Local Thermal Equilibrium (NLTE) where the radiation field at a given place is modified by its surrounding radiation. The model calculation of the NLTE radiative transfer is challenging and consumes enormous computational resources. The scattering process working well in this region causes complicated frequency re-distribution, which alters the emergent intensity in the line wing. Moreover, the optically thick formation properties of several chromospheric lines make the modeling difficult. See Sec. 1.3.3 for some details of the modeling of chromospheric spectral lines.

Various chromospheric lines fall in the optical and ultra-violet (UV) wavelength regime. Ground-based telescopes are employed to observe chromospheric lines in the optical range longer than 350 nm. On the other hand, most UV lines are strongly affected by the earth's atmosphere, requiring observations from space. Much efforts have been devoted to improving modern observational instruments to record high resolution and high dispersion spectral lines. In parallel with such developments, numerical modeling of the
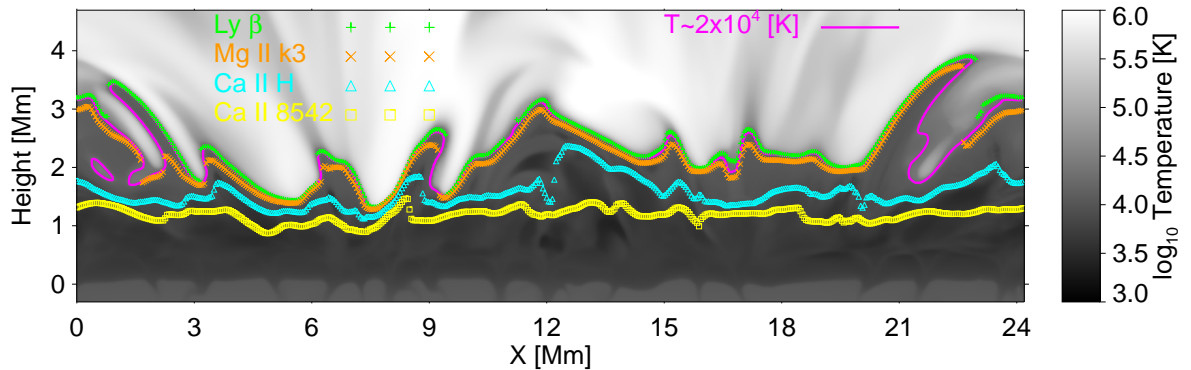
Figure 1.2: The heights where $\tau = 1$ at the line cores of the important chromospheric lines, overplotted on the temperature in the vertical cut of the 3D simulated realistic atmosphere.

chromospheric diagnostics has been developed with great efforts. Chromospheric diagnostics are reviewed by Carlsson et al. (2019), and we give some description for conventional chromospheric lines below.

Since in the optical regime, the spectral lines are less affected by the absorption in the earth's atmosphere, those lines have traditionally been obtained by ground-based telescopes. Important optical lines are the Hα 656 nm, Ca II H&K at 397 and 393 nm, Ca II 854.2 nm, and He I 1083 nm. The Hα line is an established tool to probe the mid-chromosphere. The line allows us to observe the low-temperature structure of 5-10 kK, such as prominences. The Ca II H&K lines are the resonance lines originating from the single ionized calcium. These spectral profiles give us the temperature information in the photosphere and chromosphere. When a solar flare occurs, and the lower atmosphere is heated, the two ribbon-like bright features (i.e., "flare ribbon") appear in the filtergram images including Ca II H spectral line, e.g, taken by the *Solar Optical Telescope* on board the *Hinode* satellite. The Ca II triplet lines located in the infrared regime (viz., 849.8, 854.2, and 866.2 nm), known as the Ca II IR triplet, are middle chromospheric diagnostics which form at similar height to the Hα. The Ca II K line is currently accessible by the *CHROMospheric Imaging Spectrometer* (CHROMIS) installed on the *Swedish 1m Solar Telescope* (SST, Scharmer et al., 2003). The *CRisp Imaging SpectroPolarimeter* (CRISP,

Scharmer et al., 2008) is also installed on the SST, observing the full Stokes profiles of the Hα and Ca II IR.

Furthermore, we have some UV chromospheric lines whose high resolution spectral information becomes accessible after the launch of the *Interface Region Imaging Spectrograph* (IRIS, De Pontieu et al., 2014). The space observations by the IRIS satellite prevent the UV lines from being absorbed by the earth's atmosphere. The most important IRIS chromospheric diagnostics in the UV regime is the Mg II h&k. These are the resonance lines at 280.3 and 279.6 nm, originating from the singly ionized magnesium. The lines have similar features to the Ca II H&K, and 18 times larger opacity of Mg makes the lines form higher. Other IRIS lines are the C II 133.5 nm and O I 135.56 nm. The former carbon line forms in the optically thick regime. The line often forms higher than the Mg II h&k, but sometimes lower (Rathore et al., 2015). The latter oxygen line is optically thin and less affected by the opacity broadening, hence, its line width is a suitable probe for the non-thermal velocities (Lin & Carlsson, 2015). These spectroscopic properties and diagnostic capabilities were numerically scrutinized in the series of works entitled "The formation of the IRIS diagnostics" (e.g., Leenaarts et al., 2013a).

Recent theoretical studies and analysis of space and ground-based observations of the above-mentioned spectral lines revealed dynamic chromospheric features (for review, see Carlsson et al., 2019). However, the vigorous activities revealing the chromosphere from the perspective of modeling and observations have just started, and understandings the mysterious atmospheric region is far from a satisfactory level.

In Fig. 1.2, we plot the $\tau = 1$ heights of the important optically thick chromospheric lines to which we have access (viz, Mg II k, Ca II H, and Ca II IR), overplotted on the temperature in the vertical cut of the realistic atmosphere simulated with the BIFROST code (Gudiksen et al., 2011). In this plot, we also present the $\tau = 1$ height of the Lymanβ (Lyβ) line, which we will investigate in this dissertation. Because the chromospheric diagnostics is still scarce, we have a diagnostic gap, for instance, from the formation heights of Ca II H to Mg II k, where we cannot have access via the current spectroscopic
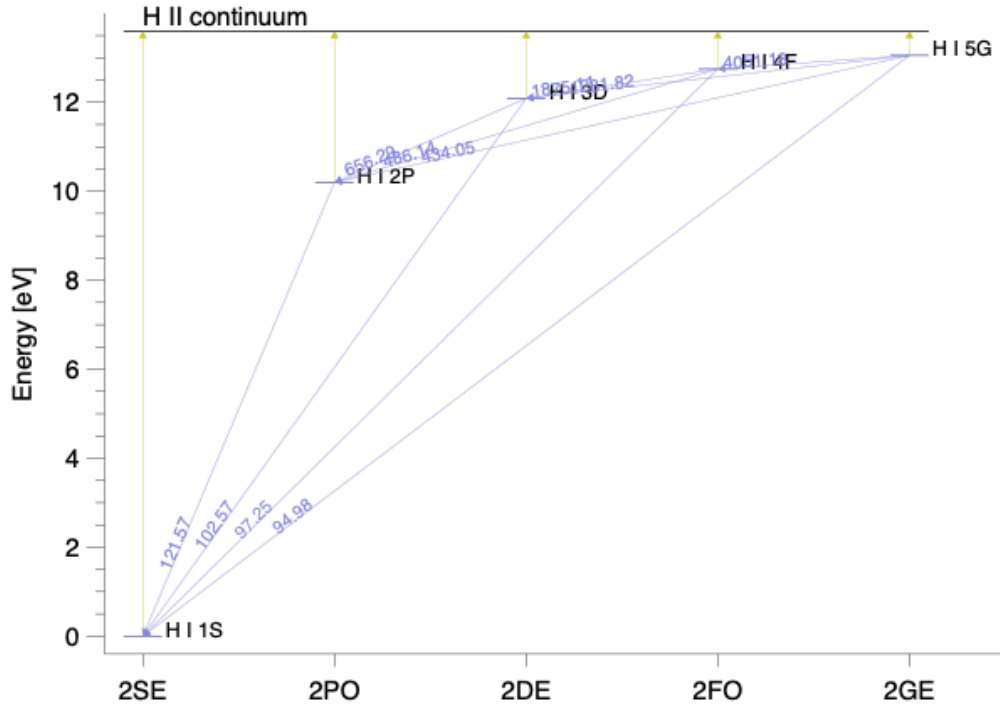
Figure 1.3: Term diagram of the six-level H atomic model used in this work.

observations. The core of Mg II k forms around T $\sim 10^4$ K and we do not have access
to the chromosphere hotter than 10^4 K. In particular, such temperature gaps appear in a
tall chromospheric structure protruding into the corona as shown, e.g., X ~ 2.5 Mm in
Fig. 1.2. Therefore, we cannot follow how such a tall chromospheric protrusion is heated
as it goes to the corona. For further exploration to the chromosphere, we need more
diagnostic tools which can bridge these missing regions.

1.3 Lyman Transitions

1.3.1 General Description

For the purpose to fill the diagnostic gaps and to achieve a better understanding of the
chromospheric structure, the hydrogen Lyman transitions are excellent candidates as new
tools to probe the gaps from Ca II H&K to Mg II h&k and beyond Mg II h&k.

13

Lyman lines are emitted by the bound-bound transitions from a bounded electron's excited state to the ground state in neutral hydrogen. Fig. 1.3 presents the term diagram of the neutral hydrogen model employed in this dissertation. This is a simplified model consisting of six levels, ten bound-bound transitions, and five bound-free transitions. When the main quantum numbers of the upper levels are n=[2,3,4, ...], the transitions are called Lyman $\alpha, \beta, \gamma, ...$, respectively. Due to the largest abundance of the neutral hydrogen in the solar atmosphere, Lyman α (Lyα), at 121.57 nm, is the brightest spectral line in the EUV regime. This emission originates from the transition from the term $1s^2S^e$ with energy 82258.211 cm^{-1} to the ground state. Lyβ at 102.57 nm is one higher Lyman line and emits from the transition from the term $2p^2P^o$ with energy 97491.219 cm^{-1} to the ground state.

As shown in Fig. 1.2 with green symbols, the core of Lyβ forms at the upper chromosphere where temperature is $\sim 2 \times 10^4$ K (Hasegawa et al., 2020), which is higher than the core of Mg II h&k lines. The structure in which the core of the Lyman lines and Mg II k form is similar, but in some locations, for instance at the thread-like protruding structure at X $\sim$ 2.5 Mm, we can find a large deviation. Not only the line core, but the wing may also provide good diagnostics to probe the chromosphere because strong absorption at the Lyman line's core results in the formation of emission peaks, similar to h2 (k2) structure of Mg II h (k). Since the opacity at the emission peak is smaller than that of the core, these features can be potentially employed as a diagnostics of the mid-chromosphere.

Despite the mentioned potential of the Lyman transitions, their observation is scarce because they are located in the EUV regime. This lack of observations produces that we do not sufficiently understand their spectroscopic properties. For these reasons, in the following, we will review the general features of the Lyman lines inferred from the observations in the previous era, mainly with the *Solar Ultraviolet Measurements of Emitted Radiation* (SUMER, Wilhelm et al., 1995; Lemaire et al., 1997) instrument on board the *Solar and Heliospheric Observatory* (SoHO, Domingo et al., 1995) spacecraft and some modeling efforts of Lyman lines and their difficulties.

1.3.2 Observations

Since the Lyman lines fall in the EUV band, they are affected by geo-coronal absorptions in the earth's atmosphere. Spectrally resolved Lyman lines have been difficult to access until the space-born observations became available. In the 1970's, such observations were conducted by the *Laboratoire de Physique Stellaire et Planétaire* (LPSP) instrument on board the OSO-8 satellite (Lemaire et al., 1978). Until recently, the Lyman lines were regularly observed by the SUMER instrument on board the SoHO spacecraft (Domingo et al., 1995). SUMER observed a variety of Lyman lines, including Lyα and β. For observations of Lyα, a 1:10 attenuator was used to avoid saturation in the detectors due to its strong emission. However, this caused an unforeseen alteration of the line profiles (Wilhelm et al., 1995). For that reason, reliable observations of Lyα had not been done with SUMER routinely. On the other hand, Lyβ was not suffered from such unexpected alternation and was observed more frequently by the SUMER instrument.

Several authors have examined the spectral features of Lyβ. Zhang et al. (2010) studied how Lyβ responds to TR explosive events. Xia et al. (2004) analyzed the spectral lines, including Lyβ, which are sensitive to the range from chromospheric to lower-coronal temperature to investigate the dependence of the Doppler shifts on magnetic field configuration. Lyman lines were also used for observations of cool plasma in the corona, i.e., quiescent filaments and prominences (Heinzel et al., 2001; Gunár et al., 2007; Vial et al., 2007), and these were compared with simulated spectra emerging from the slab modeling (Heinzel et al., 2001; Heinzel & Anzer, 2001; Heinzel et al., 2005; Gunár et al., 2008).

Although the routine Lyα observations were difficult to execute, there were some efforts to obtain the Lyα spectra with the SUMER. Curdt et al. (2008) performed a non-routine operation with the sit-and-stare mode, in which they partially opened the aperture door to decrease the number of incoming photons. This ingenuity enabled the observation of less altered Lyα spectra, providing a direct comparison between Lyα and β, such as the center-to-limb variation and the profile shapes of Lyα and β. The same technique
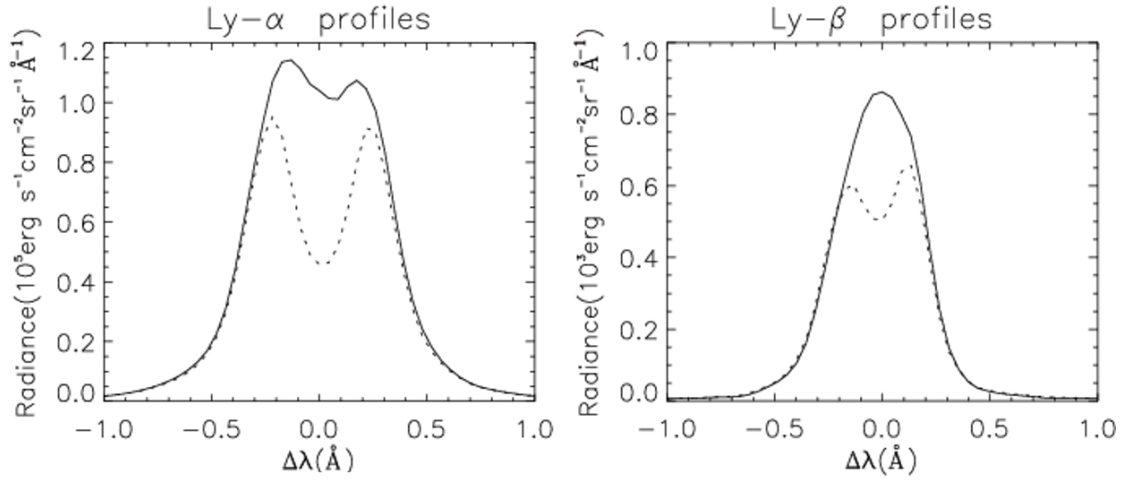
Figure 1.4: Averaged spectra of Lyα (left) and β (right) nearly simultaneously observed with the SUMER instrument. Dashed lines are mean spectra with deep central reversal, and solid lines are mean spectra less reversed. The content was adapted from Fig. 3 of Tian et al. (2009a).

was used to obtain raster scan in the disk center quiet sun (Tian et al., 2009a) and in the polar coronal holes (Tian et al., 2009b). Tian et al. (2009a) found that almost all the Lyα have self-reversed core, whereas 17% of Lyβ are not reversed in the network structure. The reason might be because the lower opacity of the upper level of Lyβ than that of Lyα. Fig. 1.4 has come from Tian et al. (2009a), showing the mean Lyα and β spectral profiles whose core reversals are deep (dashed) and shallow (solid), respectively. These averaged spectra also show the opposite asymmetry of emission peaks; the emission peak at the shorter (blue-ward) wavelength in the Lyα spectral profile tends to be stronger, whereas the emission peak at the longer (red-ward) wavelength in the Lyβ spectral profile is prone to be stronger. The red-asymmetry observed in Lyβ is also found in the higher Lyman transitions (Warren et al., 1998). However, the reason why a different behaviour in the asymmetry is produced between Lyα and β (and higher Lyman lines) has not been revealed yet. Gunár et al. (2007) surveyed the behaviour of Lyα and β profiles in the prominence with 1D slab modeling and suggested that the ingredients of this discrepancy are the complex velocity distribution in the LOS and difference of the core opacity.

Recently, a sounding rocket experiment, *Chromospheric Lyman Alpha SpectroPolarimeter* (CLASP, Kano et al., 2017) performed 5 minutes Lyα observations, mainly on the solar limb. This mission was dedicated to chromospheric magnetic field measurement by measuring the linear polarization due to the Hanle effect (Kano et al., 2017; Ishikawa et al., 2017). Trujillo Bueno et al. (2018) demonstrated that the geometric corrugation of the TR has a substantial impact on the center-to-limb variations of the linear polarization signals. With the slit-jaw images, Kubo et al. (2016) found propagations of intensity disturbances, which indicate slow-propagating magneto-acoustic waves. The high cadence sit-and-stare observations of the Lyα Stokes I signals were exploited for the detection of the high-frequency waves propagating in spicules (Yoshida et al., 2019).

Because the SUMER observations were basically limited to the quiet Sun, the responses of the Lyman lines to active phenomena have hardly been investigated. Furthermore, the limited raster-scanned regions and the short observation time of the CLASP observation restrict the understandings of the general spectral features of the Lyα in a wide range of the atmospheric scenario. Therefore, even for Lyβ, the available spectroscopic observations of the Lyman transitions are still insufficient.

1.3.3   Modeling

Modeling the formation of strong chromospheric lines, including Lyman lines, is a challenging task, mainly because of the following reasons:

1. the NLTE radiative transfer,

2. the optically thick formation, and

3. the frequency redistribution effects occurring in a scattering process.

In the photosphere where density is sufficiently high, atomic transitions are governed by the collisional rate rather than the radiative rate. In the case, we can assume the transitions are in the LTE, and the populations are determined by the local atmospheric condi-

tions, as formulated by the Saha equation for the ionization state:

$$\frac{N_{j+1}N_e}{N_j} = 2\frac{U_{j+1}(T)}{U_j(T)}\left(\frac{2\pi m_e kT}{h^2}\right)^{3/2}e^{-\chi_{j,j+1}/kT} \tag{1.2}$$

where N_j is the number density of the given atom in the j$^{\text{th}}$ stage of ionization, N_e is the electron density, U_j is the partition function dependent only on the temperature T, and $\chi_{j,j+1}$ is the energy required to ionize the given atom, and by the Boltzmann equation for the excited state:

$$N_i = \frac{N}{U}g_i e^{E_i/kT} \tag{1.3}$$

where E_i is the energy for the atomic state *i*, N is the total population, $U = \sum g_i e^{-E_i/kT}$, and g_i is the statistical weight (Rybicki & Lightman, 1986). The above set of equations means that the population of the atomic state, and thus the radiation field, is determined only by the local temperature in LTE. The LTE approximation makes the radiative transfer processes easy. However, the departure from the LTE condition makes the situation more difficult. The plasma is less dense in the chromosphere, and radiation is the predominant process for the atomic level transitions. As the atomic population is affected by the radiation coming from a distant atmospheric domain, the radiation field is not determined by the local condition. The NLTE nature of the chromospheric plasma makes the modeling and interpretation of chromospheric spectra challenging.

In the TR or the tenuous corona, most emitted photons freely escape, i.e., optically thin regime. In this case, the emergent intensity can be approximated as (see Sec. 3.1 in Del Zanna & Mason, 2018):

$$I_{\nu_{ij}} = \frac{h\nu_{ij}}{4\pi}\int N_j(Z^{+r})A_{ij}ds, \tag{1.4}$$

where A_{ij} is the Einstein's A value, i.e., the probability for the spontaneous emission between levels i and j, and Z^{+r} stands for the element of atomic number Z ionized r times,

and can be derived with the atomic database *CHIANTI* (Dere et al., 1997). In contrast, some strong chromospheric lines, such as the Lyman transitions, form in optically thick regime due to the high abundance of atomic species, and the approximation of Eq. (1.4) is not valid.

The strong chromospheric lines have other difficulties. A scattering process modifies the frequency distribution of inward emission. When the scattering is weak, i.e., the time scale for a scattering process is short, we can assume the frequency distribution of inward and outward emission is identical, and such process is the complete redistribution (CRD). On the other hand, when the time scale for scattering is large, the outward emission and its frequency distribution are affected by collisions. This effect, i.e., the partial redistribution (PRD), is significant in the computation of the radiative transfer, especially in the line wing and the geometry of the solar limb observation.

For the difficulties mentioned above, the Lyman line spectra should be modeled with spectral synthesis by solving the full radiative transfer equations and a set of rate equations of each atomic level, considering the PRD effects. As the set of equations is much enormous and complicated, the synthesis of a chromospheric spectral line is challenging.

There has been some efforts in modeling the Lyman transitions. Since radiative energy loss in the Lyman lines (especially Lyα) have an essential role in the energy balance of the TR, modeling the Lyman transitions are necessary to construct the static model atmosphere. In this regards, Fontenla et al. (1990) created a standard static model atmosphere, solving the radiative transfer equation and statistical equilibrium equation, including the ambipolar diffusion velocity term for hydrogen. Their models with hydrogen diffusion produced Lyman lines and continua of the same magnitude of those observed, without the temperature plateau at T $\sim$ 20,000 K introduced in Vernazza et al. (1981). Fontenla et al. (1991) applied the modeling on various atmospheric features, i.e., the network cell center, an average area, the bright network, and a plage. Finally, Fontenla et al. (1993) included not only the diffusion of hydrogen but also of helium, reproducing the intensity at the emission peaks in the wing of Lyα consistent with observations.

However, the solar atmosphere, especially the chromosphere, is essentially inhomogeneous and time-dependent so that the static and average model atmosphere can fail to reproduce many features in the chromospheric spectral lines (Carlsson et al., 2019). We need realistic 3D atmospheric scenarios for the line synthesis with much higher accuracy. In this sense, Schmit et al. (2017) synthesized the Lyα spectra with a snapshot of the realistic atmosphere computed with the BIFROST code and revealed its spectral feature. Regarding Lyβ, however, such inspections are scarce, except for the work accomplished in this thesis (see Chap. 2) and by Hasegawa et al. (2020).

1.4 Purposes of this Dissertation

As stated earlier, the Lyman transitions are excellent candidates for further chromospheric diagnostics. However, due to the lack of observations and the difficulties in modeling them, their spectroscopic features are not well understood.

Motivated by that situation, we dedicate this dissertation to numerically simulate the Lyman lines by solving the full radiative transfer with a realistic 3D MHD atmospheric model. Furthermore, we characterize spectral features of the lines, i.e., the line shape, and reveal the relationship between those features and the atmospheric structure.

In particular, we attempt to address following objectives:

1. We estimate to which temperature structure the Lyman line's core and wing have sensitivities. We characterize the simulated line shape, relate them to the height variation of thermal parameters. We also analyze the observed spectra, link them to photospheric magnetic field, and compare them with the simulated spectra. With these analyses, we evaluate the capabilities of the lines to diagnose the chromospheric plasma conditions and dynamics. As stated earlier, the wing of a spectral line forms at the lower region than the core. Therefore, characterizing the whole Lyman spectral profile, including its core and wing, effectively helps us fill the diagnostic gaps.
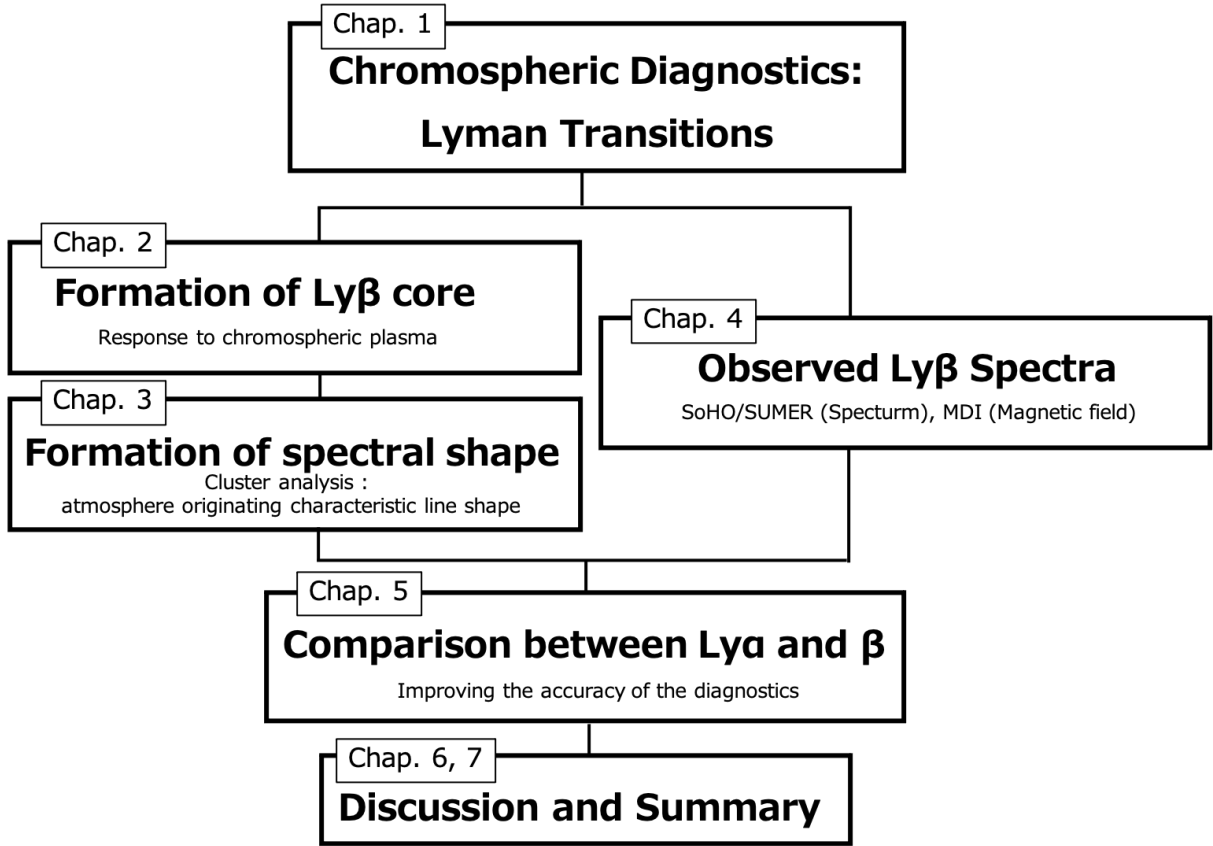
Figure 1.5: The flow of contents in this dissertation.

2. We scrutinize how the asymmetries in the Lyman line emission peaks form. We look for conditions to reproduce the opposite asymmetries of Lyα and β, which is observationally reported by multiple authors (e.g., Tian et al., 2009a). We discuss how the asymmetry gives a constraint in the atmospheric stratification in the quiet Sun, and how useful the asymmetry is as chromospheric diagnostics.

As mentioned in Sec. 1.3.3, detailed calculations have been done for Lyα by Schmit et al. (2017). Here, we will mainly concentrate on Lyβ. However, in Chap. 5, we will add Lyα to our analyses.

The dissertation is organized with the following contents, as displayed in the chart in Fig. 1.5. In Chapter 2, we employ the modern techniques of radiative transfer computation and the state-of-the-art realistic 3D model of the solar atmosphere to synthesize the Lyβ emergent spectra numerically. With these results, we scrutinize the general forma-

tion properties of Lyβ. Chapter 3 investigates the statistical properties of the shapes of synthesized Lyβ, including its wings as responses to the various atmospheric scenarios in the 3D model atmosphere. For this purpose, we take advantage of the cluster analysis and organize the synthesized spectra into families based on their line shapes. Although the observations of Lyman transitions have been limited so far, we identify four raster maps of Lyβ in the SUMER data archive appropriate for the cluster analysis. In Chapter 4, we classify the observed spectra in the same manner as the synthesized spectra and deduce the relationship between the line shapes and atmospheric environment. We additionally compare the results obtained from synthesized and observed spectra. In Chapter 5, we also take into account the Lyα and investigate the mechanism that causes the different behaviour in asymmetry of Lyα and β. Chapter 6 provides a general discussion on the results obtained until then, mentioning our visions for the next generation space-born spectroscopic observations. Finally we give the concluding remarks in Chapter 7.

Chapter 2

Spectral Synthesis of Lyman β

In this chapter, we numerically synthesize the spectra of a hydrogen Lyβ transition and examine general spectroscopic properties of the spectral line, especially of its core. Properties of wings are more focused in the following chapters. For this purpose, we make use of a 1D semi-empirical atmospheric model and a 3D realistic MHD simulation that reproduces solar phenomena at high level of accuracy. We also use a state-of-the-art numerical codes that allow generating the solar spectrum from those atmospheric scenarios.

2.1 Introduction

For computing the strong NLTE chromospheric lines, we have to solve a huge set of equations including the radiative transfer equations and rate equations for each atom of interest. By now, much efforts are devoted to simpler formalism of these equations. Rybicki & Hummer (1992) formulated the multi-level accelerated Λ-iteration (MALI) for the complete re-distribution (CRD) formalism. Uitenbroek (2001) improved the MALI method by implementing the partial re-distrbution (PRD) formalism. The formalism is implemented in the numerical code *RH*, which is a standard for the computation of the radiative transfer including the PRD effects. On the other hand, the radiative transfer code *multi* (Carlsson, 1986) is also employed for the computation of the spectra. The code is further developed to *multi3D* and is extended for the 3D radiative transfer (Leenaarts &

Carlsson, 2009). For the computation of the 3D radiative transfer, the code *multi3D* is de-facto standard in present, whereas the *RH* is preferable for the computation considering the effects of PRD.

These radiative transfer codes have been employed for characterizations of the chromospheric spectral lines which have to be considered in the NLTE regime. With the formalism introduced by Uitenbroek (2001), Uitenbroek (2006) computed the chromospheric spectra of Na I D and Ca II IR with semi-empirical 1D atmosphere and a snapshot of the 3D atmosphere by Asplund et al. (2000). The synthetic reproduction of the Hα had not corresponded to the observation till Leenaarts et al. (2012), who included the 3D radiative transfer. The emergent intensity maps reproduced by the authors are dominated by the dark fibrils which had not been reproduced by the synthesis and are often observed by the Hα observations. Among the IRIS spectral lines investigated in the series of works entitled "The formation of the IRIS diagnostics", Leenaarts et al. (2013a) demonstrated the importance of the 3D effects in the Mg II h&k transitions. However, it was very difficult to include the 3D NLTE radiative transfer and the PRD effects due to the demand of the huge computational resources. Recently, Sukhorukov & Leenaarts (2017) implemented the PRD formalism in the 3D NLTE radiative transfer solved by *Multi3D*. Such a simultaneous treatment was also considered for Lyα and Mg II h&k by Schmit et al. (2017) and for Ca II H&K by Bjørgen et al. (2018).

2.2   Method

In our study, we employ the numerical code *RH* to conduct a NLTE line synthesis with the PRD effects. We assume the plane-parallel geometry in our computations, i.e., the 1D radiative transfer.

2.2.1 Spectral Line Synthesis : *RH*

To derive the emergent intensity, we have to simultaneously solve the radiative transfer equation:

$$\frac{1}{\mu}\frac{dI_\nu}{d\tau_\nu} = S_\nu - I_\nu \qquad (2.1)$$

and the equation of statistical equilibrium for each atomic level i:

$$\sum_{j\neq i}^{N} n_j P_{ji} - n_i \sum_{j\neq i}^{N} P_{ij} = 0. \qquad (2.2)$$

In Eq. (2.1), $\mu = \cos\theta$ where θ is a heliocentric angle. I_ν, S_ν, and τ_ν are intensity, source function, and an optical depth at a given wavelength ν, respectively. In Eq. (2.2), j is any atomic level other than i, n_i (n_j) is the atomic population of level i (j), N is the total number of atomic levels considered, and P_{ij} is a transition probability between level i and j:

$$P_{ij} = A_{ij} + J_\nu B_{ij} + C_{ij}, \qquad (2.3)$$

where A_{ij}, B_{ij} are the Einstein's coefficients for spontaneous and stimulated transitions, and C_{ij} is the collisional transition rate. J_ν is the angle-averaged mean intensity:

$$J_\nu = \frac{1}{4\pi} \int I_\nu d\Omega, \qquad (2.4)$$

where Ω is the solid angle. The intensity in Eq. (2.1) relates to the source function via J_ν, and the change in the atomic population modifies the source function in the NLTE regime. Therefore, these equations are linked to each other and they need to be solved iteratively until we reach a compatible solution between the radiation field and the atomic level populations. For this reason, solving these equations generally requires enormous

computational resources.

When photons are coherently scattered, these are affected by redistribution of frequency (i.e., PRD effects). Here, we formulate the PRD effects on the line radiative transfer based on Uitenbroek (2001). The emission profile ratio of the transition from an atomic level i to j, i.e., $\rho_{ij} \equiv \psi_{ij}/\phi_{ij}$ where ψ_{ij} and ϕ_{ij} are the emission and absorption profiles respectively, is formulated as:

$$\rho_{ij}(\nu, \mathbf{n}) = 1 + \frac{\Sigma_{k<j} n_k B_{kj}}{n_j P_j} \oint \frac{d\Omega'}{4\pi} \int d\nu' I(\nu', \mathbf{n}') \left[\frac{R_{kji}(\nu, \mathbf{n}; \nu', \mathbf{n}')}{\phi_{ij}(\nu, \mathbf{n})} - \phi_{kj}(\nu', \mathbf{n}') \right] \quad (2.5)$$

where R_{kji} is the generalized laboratory frame redistribution function. In the case where the scattering is not coherent, i.e., the CRD case, $R_{kji} = \phi_{kj}\phi_{ij}$ and, thus, $\phi_{ij} = \psi_{ij}$. When we assume that the lower level broadening in the atomic frame can be neglected and the CRD in the atomic frame can be approximated by that in the laboratory frame, R_{kji} yields to

$$R_{kji} = \gamma R_{kji}^{II} + (1 - \gamma)\phi_{kj}\phi_{ij} \quad (2.6)$$

where γ is the coherency fraction:

$$\gamma = \frac{P_j}{P_j + Q_j^E} \quad (2.7)$$

and Q_j^E is the upper level rate of the elastic collision. When we neglect the cross redistribution where k$\neq$i and write the redistribution function as R^{II}, the emission profile ratio is:

$$\begin{aligned}
\rho_{ij}(\nu, \mathbf{n}) &= 1 + \gamma \frac{n_i B_{ij}}{n_j P_j} \oint \frac{d\Omega'}{4\pi} \int d\nu' I(\nu', \mathbf{n}') \\
&\times \left[\frac{R^{II}(\nu, \mathbf{n}; \nu', \mathbf{n}')}{\phi_{ij}(\nu, \mathbf{n})} - \phi_{ij}(\nu', \mathbf{n}') \right].
\end{aligned} \quad (2.8)$$

Eq. (2.8) can be simplified if there are no bulk flows and thus ϕ does not depend on the
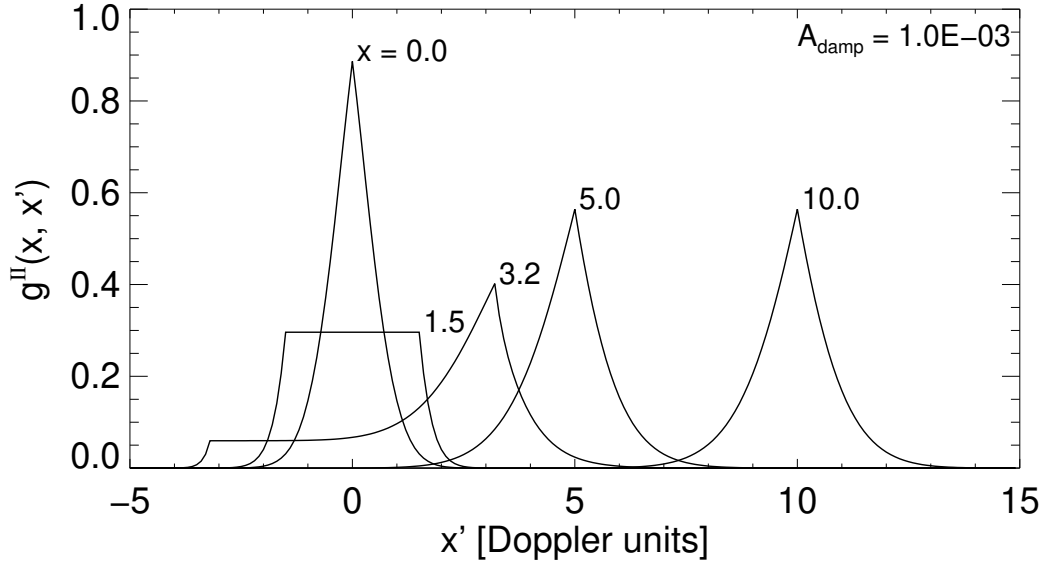
Figure 2.1: The re-distribution function normalized by an absorption profile (i.e., g^{II}) for a damping parameter of 10^{-3} and emission frequencies are 0, 1.5, 3.2, 5.0, and 10.0 in Doppler units. The plot is courtesy of H. Uitenbroek.

direction $\mathbf{n}$. In this case, we can assume an isotropic radiation field and Eq. (2.8) can be rewritten with the mean intensity $J = \frac{1}{4\pi} \int I d\Omega$:

$$\rho_{ij}(\nu) = 1 + \gamma \frac{n_i B_{ij}}{n_j P_j} \int \left(g^{II}(\nu, \nu') - \phi_{ij}(\nu') \right) J(\nu') d\nu' \qquad (2.9)$$

where $g^{II} \equiv R^{II}/\phi$ determines how the intensities are re-distributed. This is the formalism of the angle-averaged PRD. Examples of the profiles of $g^{II}(\nu, \nu')$ for a damping parameter of 10^{-3} and five given emission frequencies are shown in Fig. 2.1. In this study, we go through the results based on the angle-averaged PRD, although we briefly discuss in Sec. 6.5 the most general case, i.e., the angle-dependent PRD.

In *RH*, the NLTE problems considering PRD effects are solved with the following iterative steps:

1. An ordered list of all the necessary wavelengths is determined and the set of active transitions is stored.

2. The initial conditions for the atomic level populations are set with assumptions of LTE or zero-radiation field. An emission profile ratio ρ_{ij} is initially set as unity.

3. With the initial conditions for the populations and the emission profile ratio, opacity, emissivity, and $g_{ij} = (g_i/g_j)\rho_{ij}$ are computed, where g_i is the statistical weight of the level i.

4. The formal solution for the intensity is computed. With this solution, a set of pre-conditioned statistical equilibrium equations is solved and the populations are updated.

5. While the population in the previous step is kept unchanged, the intensity is redistributed in wavelength and the emission profile ratios are updated for the PRD transitions.

6. Steps 4 and 5 are iterated until a convergence condition is met.

For the detailed formulations of the *RH* method, see Uitenbroek (2001).

2.2.2 Model Atom

We used a H atomic model composed of six levels including the H II ground state, 10 bound-bound transitions, and five bound-free transitions, for computing the H populations and synthesizing the Lyman-series transitions. The term diagram of the atom is presented in Fig. 1.3 in the previous chapter.

For the computation of the continuum background opacity, we use a standard choice of 11 atom and 12 molecule models that are included in the *RH* source package. The atomic abundance values are taken from Asplund et al. (2009).

2.2.3 Model Atmosphere

Model atmospheres are used when we compute the transportation of radiations and derive the emergent spectra. In this study, we employed two types of model atmospheres for
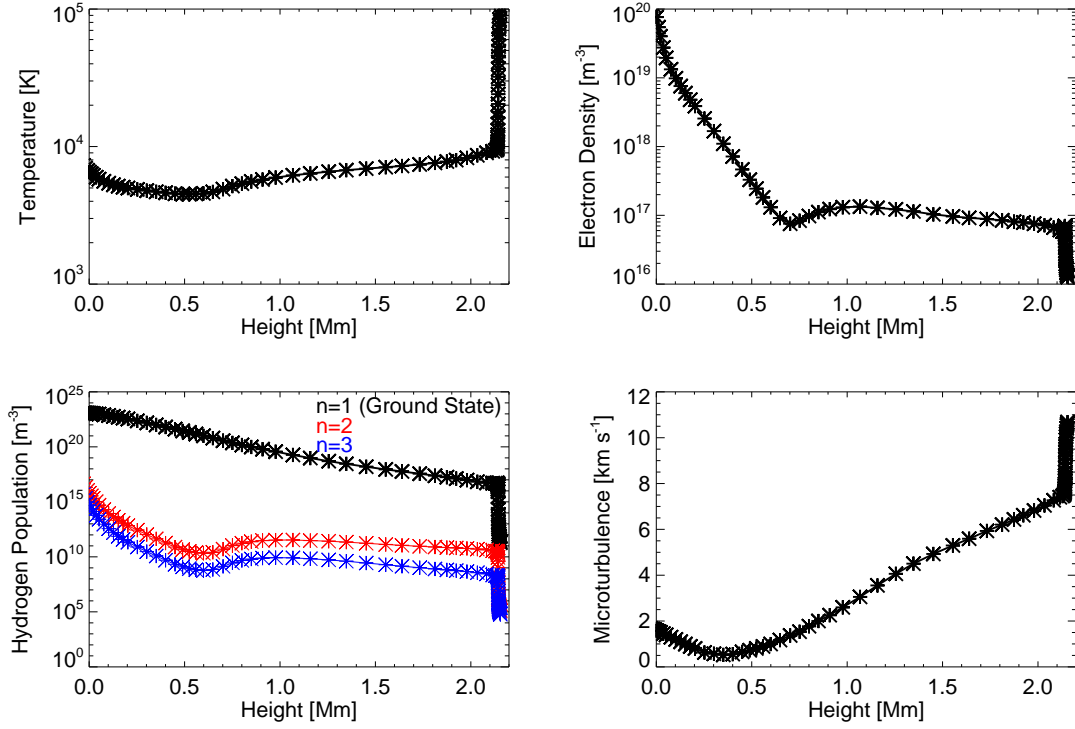
Figure 2.2: Height dependence of the physical parameters in the FAL-C atmospheric model. Temperature (top-left), electron density (top-right), hydrogen populations where n=1 is the ground state, n=2 is the upper state of the Lyα transition, and n=3 is the upper state of the Lyβ transition (bottom-left), and microturbulence (bottom-right).

different purposes. At the beginning, we used a semi-empirical 1D atmospheric model, which is the model C presented in Fontenla et al. (1993) and is conventionally called FAL-C. The atmosphere was employed for various exercises like determining the best *RH* configuration or analyzing the sensitivity of the spectral lines to the atmosphere. The FAL-C model represents the vertical stratifications of the atmosphere with which the results of the NLTE radiative transfer computation match the spatially and temporally averaged observation of UV spectra in the quiet Sun. We employed the FAL-C model included in the *RH* library. The height distributions of physical parameters, i.e., temperature, electron density, hydrogen populations, and microturbulence are presented in Fig. 2.2. In the bottom left panel, populations of the neutral hydrogen at the ground state (n=1 where n is the main quantum number), the upper state of the Lyα transition (n=2), and that of the Lyβ transition (n=3) are plotted. The vertical velocity is zero at any heights.

29

Later on, we used the realistic 3D quiet Sun atmosphere for further analyses such as the examination of diagnostic capabilities for the spectral lines of interest. We employed the snapshot 385 of the radiative MHD simulation that represents a chromospheric enhanced network structure (Carlsson et al., 2016) and it was computed with the numerical code BIFROST (Gudiksen et al., 2011). The same snapshot has been used in multiple works performing the synthesis of spectral lines (among others, Leenaarts et al., 2015; Quintero Noda et al., 2016; Štěpán & Trujillo Bueno, 2016; Sukhorukov & Leenaarts, 2017). The 3D atmosphere comprehends from the upper convection zone to the lower corona with a total size of $24 \times 24 \times 16.8$ Mm composed of $504 \times 504 \times 496$ grid cells. The grids are equidistant in the horizontal direction with the interval of 48 km and non-uniformly spaced in the vertical direction. In order to save computational time, we eliminate the lower corona from the atmosphere and use the cut of the vertical domain that goes from z=-0.5 to 5 Mm, with z=0 the solar optical surface where optical depth at the wavelength of 5000 Å is unity on average (i.e., photosphere), because the Lyman lines are scarcely affected by the upper part of the simulation domain. The isothermal surface is shown in Fig. 2.3, indicating the structure of bipolar magnetic loops.

2.3 Results

2.3.1 Determination of the optimum configuration

We started with some exercises to determine the optimum setup for our computation of radiative transfer and the synthesis of Lyβ. Here, we intended to define an accurate but computationally efficient configuration which was used for more computationally consuming tasks, i.e., the synthesis with the 3D BIFROST simulations. In the tests below, we employed the 1D FAL-C atmosphere.
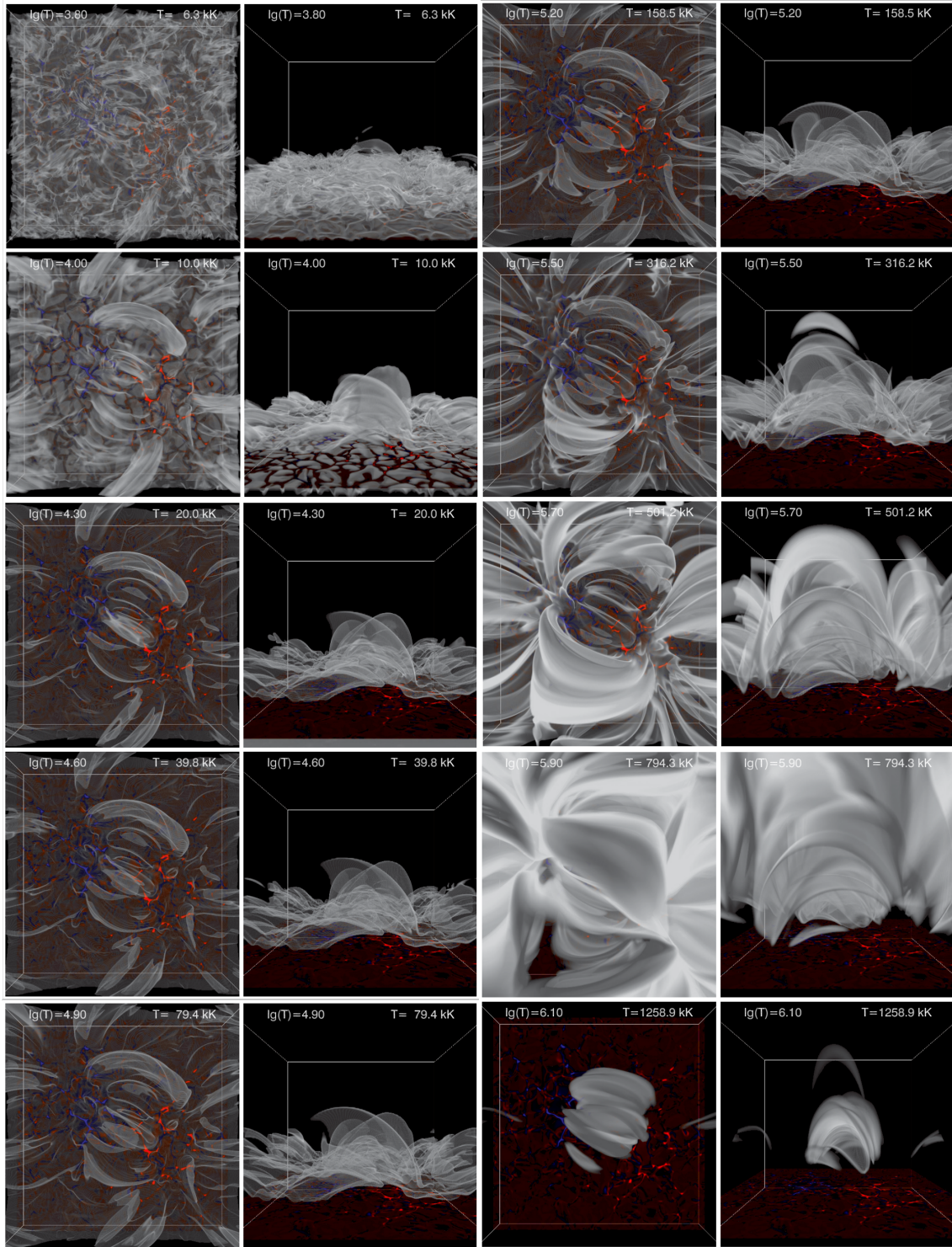
Figure 2.3: The structure of the 3D realistic atmosphere representing an enhanced network from (first and third columns) top and (second and fourth column) side view. The constant temperature surface is displayed with white surface. The distribution of (red) positive and (blue) negative magnetic flux at the photosphere is also visualized. The content was adapted from Fig. 11 and 12 of Carlsson et al. (2016).
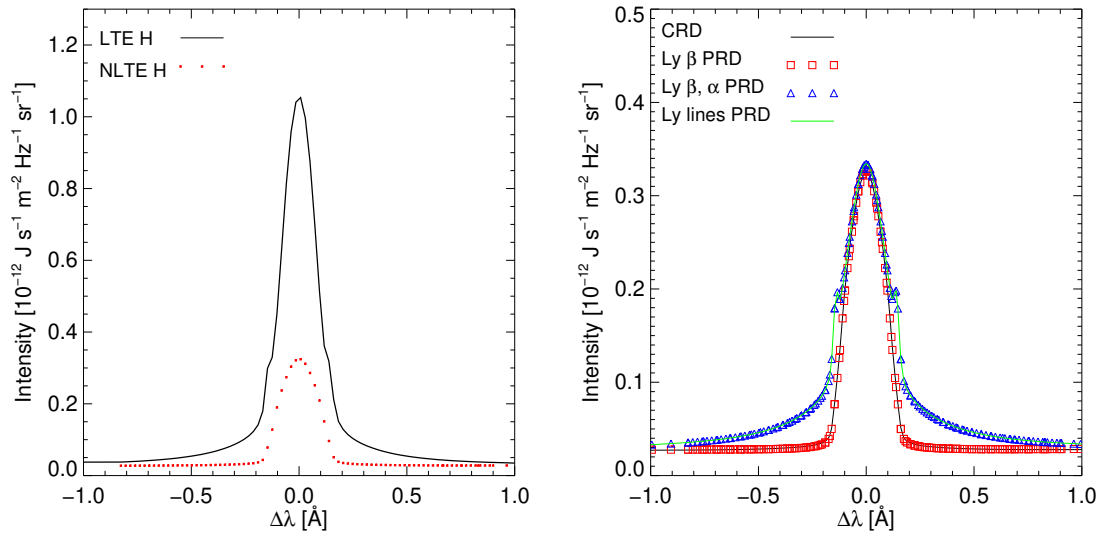
Figure 2.4: Left panel displays spectral profiles of Lyβ computed with LTE (black solid) and NLTE (red dots) populations of H. Right panel shows the same profiles computed under four different conditions regarding the frequency redistribution: all Lyman transitions are treated as CRD (black solid), only Lyβ transition is in PRD (red square), Lyα and β transitions are in PRD (blue triangle), and all Lyman lines are treated as PRD (green solid). The zero in the x-axis is set to the rest wavelength of Lyβ.

Effects of NLTE hydrogen populations

We checked how the NLTE H populations modify the Lyβ spectral line. The left panel of Fig. 2.4 displays the comparison of the spectral lines synthesized with LTE (black solid) and NLTE (red dots) H. The NLTE profile largely deviates from the LTE case both in the core and the wings. The line core intensity in NLTE is reduced to one-third of that in LTE. This is because the NLTE source function is usually smaller than that in LTE (i.e., the Planck function) due to the photon loss (Carlsson et al., 2019). This result proves that considering NLTE for computing the H populations is essential for solving the Lyβ transition and, hence, we need to consider them for an accurate synthesis.

PRD Effects of Lyman lines

We examined the impact of PRD effects for hydrogen Lyman transitions on the Lyβ spectral profile. Solving, as baseline configuration, the H populations in NLTE, we compared

four different cases. First, all Lyman transitions in the H atomic model (i.e., Lyα, β, γ, and δ) are considered under the CRD approximation. Second, only Lyβ is computed considering PRD effects. Third, PRD effects are included when computing Lyα and β. Finally, all Lyman transitions are computed taking into account PRD.

The right panel of Fig. 2.4 displays the synthesized Lyβ in the four cases. The results can be combined into two groups: whether PRD effects of Lyα are considered or not. Including the PRD effects only on Lyβ just slightly modifies the intensity profile (compare the black solid and the red squares). However, when Lyα is treated under the PRD regime (blue triangles), the intensity in the wing is remarkably altered. The line core intensity is barely affected by the Lyα PRD effects because the impact of the PRD effect appears mostly in the wings. Finally, even if additional Lyman transitions (i.e., Ly γ and δ) are considered under PRD (solid green), the Lyβ spectrum is not affected. Thus, for the optimal computational configuration, it is sufficient to consider PRD effects only for the Lyα and β transitions.

Carbon Continuum

The continuum emission in the neighborhood of 1025 Å is dominated by the ground state continua of carbon (Vernazza et al., 1981), which covers $\lambda \leq 1098$ Å and forms in the height range from 0.9 to 1.3 Mm. We tested the impact of solving the C populations under the NLTE regime on the Lyβ spectra. Figure 2.5 compares the Lyβ intensity profiles computed with C in LTE (black solid) and NLTE (red square). While considering NLTE C reduces the intensity of the wings of the spectral line, it does not change the intensity at the line core. Accordingly, as we focus on the central part of the spectral line in this chapter, we are going to simplify the synthesis process assuming C in LTE.
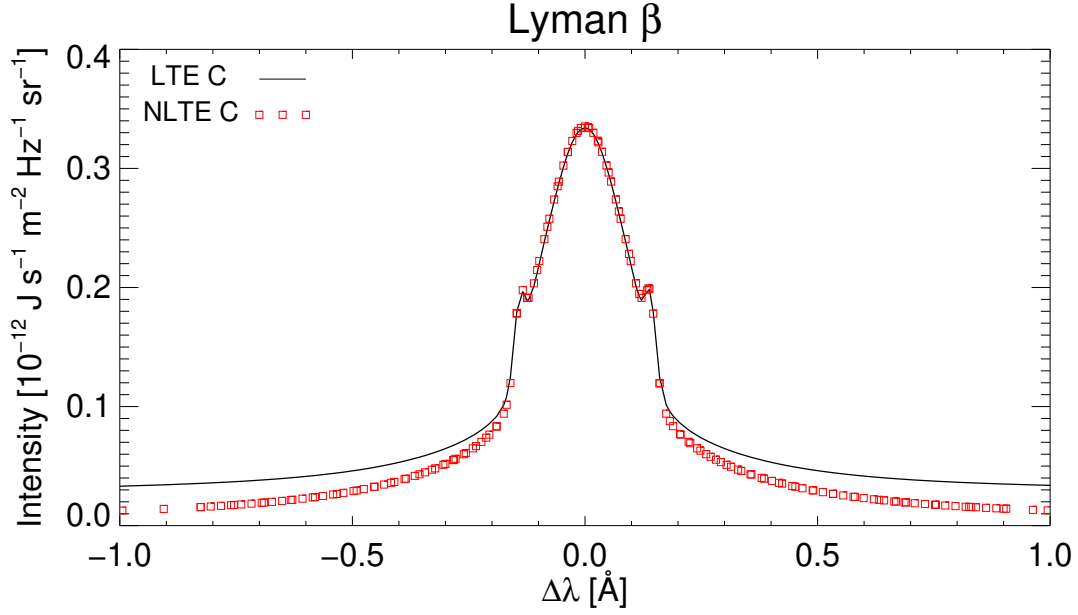
Figure 2.5: Emergent intensity profiles of Lyβ computed with LTE (black solid) and NLTE (red square) populations of C.

2.3.2 Line Formation in the 1D Atmosphere

We have determined the optimum configuration for the synthesis of Lyβ. From now on, with that optimized configuration, we study the properties of Lyβ formation using the semi-empirical 1D FAL-C atmosphere.

Formation Height

We estimated the height where the optical depth becomes unity in the Lyβ spectrum. The results are shown in Fig. 2.6. The EUV continuum forms around 1 Mm while Lyβ line core wavelengths reach up to 2.1 Mm height, which almost corresponds to the top boundary of the FAL-C atmosphere, i.e., upper chromosphere. The $\tau = 1$ height in the range of ± 0.12 Å from the line core is flat because the temperature gradient at the height is very large. The formation height sharply drops for larger $\Delta\lambda$, but the gradient becomes small at further $\Delta\lambda$ than $\pm$ 0.15 Å.
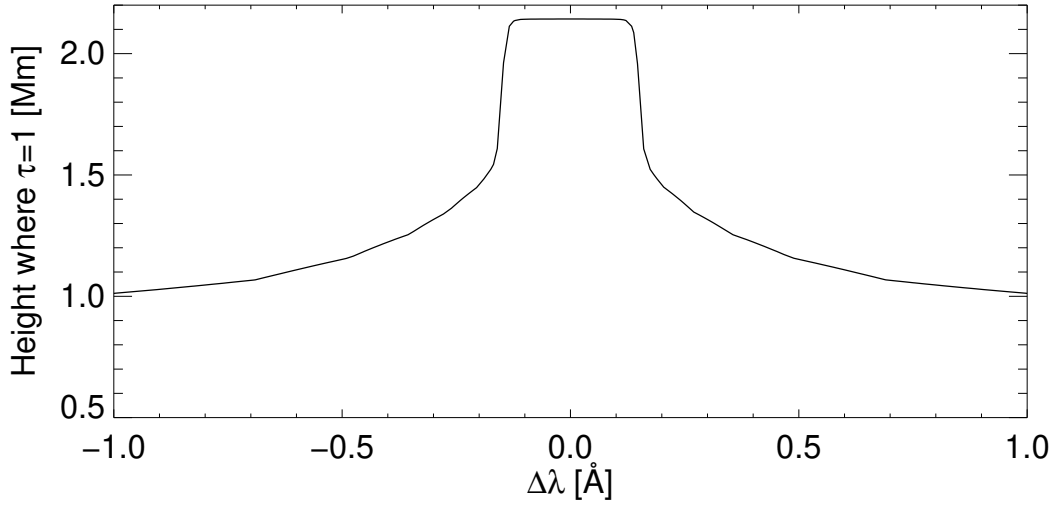
Figure 2.6: The height where $\tau = 1$ in the FAL-C atmosphere.

Response Function

We evaluated the sensitivity of the spectral lines to specific atmospheric parameters, e.g., temperature, electron density, and LOS velocity. For this purpose, we derived the response function (RF, Landi Degl'Innocenti & Landi Degl'Innocenti, 1977). The RF ($\mathbf{R}$) is determined by the modification of the intensity (δI) caused by a perturbation (δx) introduced on an atmospheric parameter (x). This is formulated as:

$$\delta \mathbf{I}(\lambda) = \int_0^\infty \mathbf{R}(\lambda, z)\delta x \, dz. \qquad (2.10)$$

We computed the numerical RF following the methods used by Quintero Noda et al. (2016). The magnitudes of perturbations introduced on temperature, electron density, and LOS velocity are 1 K, 10^{16} m^{-3}, and 100 m s^{-1}, respectively. Fig. 2.7 displays the RFs for temperature (top), electron density (middle), and LOS velocity (bottom).

The RF to temperature indicates that line core wavelengths are sensitive to a very thin layer at the upper chromosphere. The shape of the RF is similar to the height where $\tau = 1$ (see Fig. 2.6). The Lyβ wings where $\Delta\lambda > 0.15$ Å are sensitive to a relatively wide height range of 1.3-1.8 Mm. The result indicates the absence of degeneracy respect
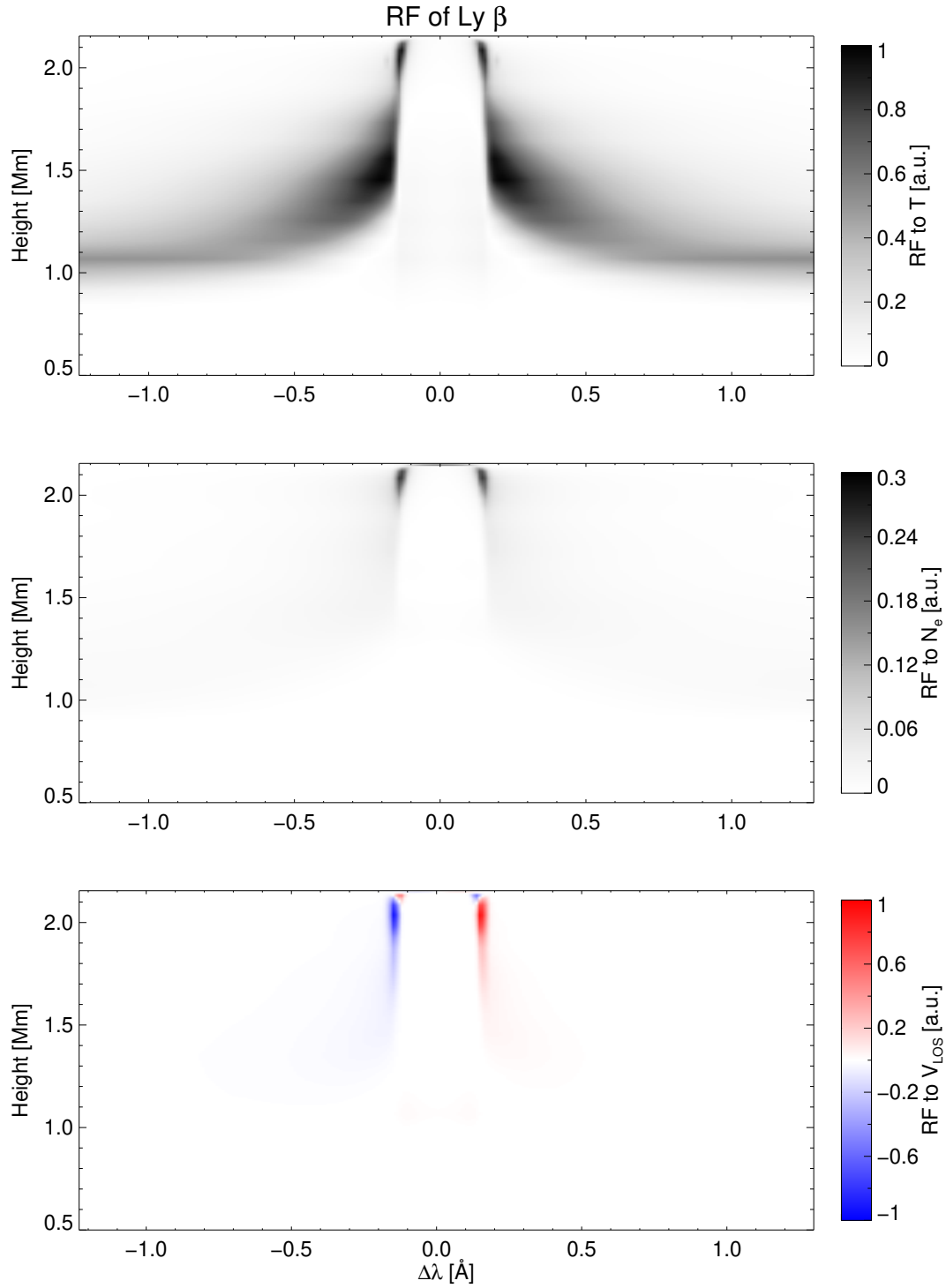
35

Figure 2.7: RFs of Lyβ to perturbations on the temperature (top), electron density (middle), and LOS velocity (bottom).

to temperature, i.e., the emergent intensity at each wavelength is only sensitive to a given range of atmospheric heights.

The RF to electron density at the core wavelength is similar to that to changes in temperature. However, when we zoom up the region around $\sim$2.1 Mm, we can find large value of the RF at the Lyβ core (i.e., $\Delta\lambda < 0.1$ Å), indicating that the line core intensity is sensitive to perturbations on the electron density at the limited thin region of its formation height, i.e., no degeneracy. This is dissimilar to the optically thin lines whose intensity is related to the electron density in the wide region. Different from the RF to temperature, there is less sensitivity to the electron density in the Lyβ wings (i.e., $\Delta\lambda > 0.15$ Å).

Concerning the RF to LOS velocity, we can see a similar behavior with the above-mentioned results, namely that the line core is sensitive to perturbations close to the upper boundary of the FAL-C atmosphere. Slightly further on the wings there is sensitive to the perturbations of the LOS velocity at $\sim$1.5-2 Mm similarly to the temperature RF. Similar to the RF to electron density, the intensities in the wings are less sensitive to the perturbations at the height of $\sim$1-1.3 Mm.

2.3.3 Line formation in the 3D realistic atmosphere

We continue examining the properties of Lyβ in a variety of atmospheric scenarios with the realistic 3D atmosphere computed with the numerical code BIFROST. We performed the spectral synthesis with the 3D atmosphere assuming the plane-parallel geometry. This means that 1D radiative transfer is solved at each pixel in the column-by-column manner.

Figure 2.8 depicts the atmospheric properties where the Lyβ core forms. The left panel displays the geometrical heights where the optical depth is unity at the Lyβ core wavelength. The distribution of the heights reflects the structure of the upper chromosphere of the model atmosphere (see also Fig. 2.3). The magnetic loop structure reaches as high as 4 Mm at the center of the field-of-view (FOV). The structure connects magnetic bipoles located around [X, Y] = [5, 14] and [16, 10] Mm. The average height where the

Lyβ core has sensitivity is $\sim$ 2.8 Mm height. At [X, Y] = [19, 4] and [2, 22] Mm, for example, we can see some protrusions whose heights reach higher than 4 Mm.

The middle panel displays the emergent intensity at the line core. In the intensity map, we can see a similar pattern to that of the formation height, where the two magnetic concentrations are connected by magnetic loops. We can see the anti-correlation between the formation height and emergent intensity. At the base of the loops where formation height is small and the magnetic field larger, Lyβ core has strong emission. On the other hand, higher-lying magnetic loops correspond to lower intensities.

We add in the right panel the temperature at the height which is shown in the left panel (i.e., $\tau = 1$ height at the line core) to investigate which kind of magnetic structure the spectral line is sensitive to. The temperature distribution looks similar to that of the emergent intensity. We can see that the temperature is higher at the footpoints of magnetic loops than in the surrounding regions. At the footpoints, the core emergent intensities are also strong. On the other hand, the temperature is low and uniform on the surface of each magnetic loop located at the center of the FOV. On average, the formation temperature of the Lyβ core is $\sim$ 23,000 K. We believe that, albeit simple, this plot provides a representative visualization of the spectral line properties in a complex scenario like the one examined here. However, we are aware that the spectral line is sensitive to the atmosphere over a given range of heights (larger than the single value we picked).

2.3.4 Diagnostic Capabilities

We assessed the capabilities of the Lyβ core to diagnose atmospheric conditions. As the Lyβ core is optically thick and is exclusively contributed by the atmospheric conditions at the thin range in the upper chromosphere, the information of gas and thermal dynamics is embedded in its spectral features (e.g., Doppler shifts).

In the beginning, we examine the capabilities of the core Doppler shifts to infer the bulk velocity along the LOS at the upper chromosphere. For deriving the Doppler shift,
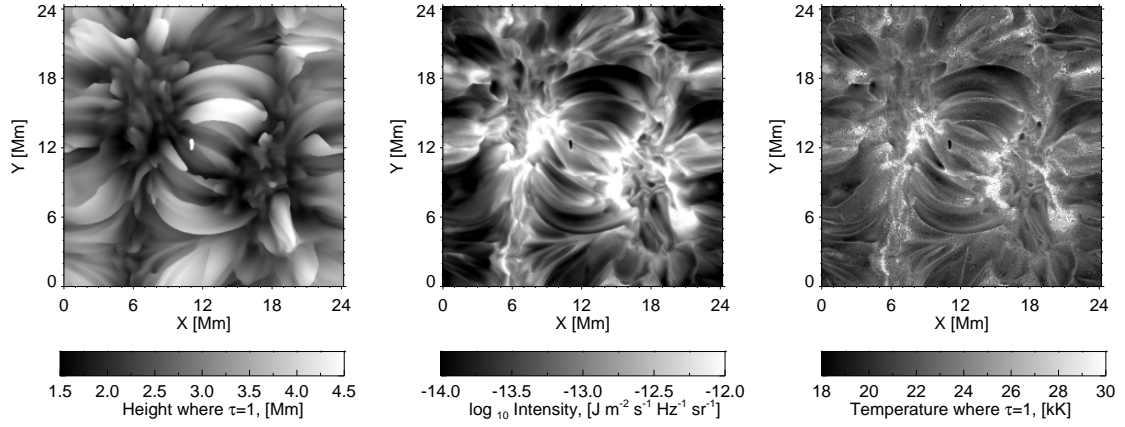
Figure 2.8: Left panel shows the geometrical height where the optical depth of Lyβ line core becomes unity. Middle panel displays the emergent intensity at the same wavelength while the rightmost panel shows the temperature at the height corresponding to the left panel in the 3D model atmosphere.

we found that the single Gaussian fitting is not appropriate, due to the intricate shapes of Lyβ profiles with multiple lobes. This might be produced by the complex LOS velocity distribution in the 3D atmosphere, including the fine-scale plasma dynamics. For this reason, we developed an algorithm to determine the line core wavelength using the following steps:

1. We computed a line core wavelength at a pixel of (x,y) = (0,0). We set an initial guess of line core extremum as one closest to the Lyβ rest wavelength.

   (a) If the spectral profile at the pixel only has a single peak, we performed a parabola fitting for several pixels in adjacent of the extremum.

   (b) Otherwise, we checked whether there are other extrema in both of shorter and longer wavelength range than the initial guess. If extrema exist in both sides, pixels between the two extrema closest to the extremum of initial guess were fitted. If not, as in the case of single peak profiles, adjacent pixels were used for a fitting.

2. We repeated the procedure for pixels in the bottom boundary (i.e., y=0) with incre-

menting x-coordinate by one. In this case, at the pixel of (x,0), an initial guess of core extremum is one closest to the fitted line core at the pixel of (x-1,0). If the core extremum is further from the rest wavelength than an arbitrary threshold, an initial guess is set as one closest to the rest wavelength. After the procedure, we repeated again for pixels in the left boundary (i.e., x=0).

3. Finally, the same procedures were applied for the profiles at the remaining pixels of (x,y). In this case, an initial guess of core extremum is one closest to the average of the fitted core wavelengths at (x-1, y) and (x, y-1). If the core extremum is further from the rest wavelength than an arbitrary threshold, an initial guess is set as one closest to the rest wavelength.

4. Doppler velocity was computed with a Doppler shift ($\Delta\lambda$) which is a difference between the detected core wavelength and the rest wavelength, as $c(\Delta\lambda/\lambda_0)$, where c is the speed of light and λ_0 is the rest wavelength.

The inferred LOS velocities derived with the method described above are shown in the left panel of Fig. 2.9. As a reference, in the middle panel we exhibit the vertical velocity in the model atmosphere at the height where $\tau = 1$ at the line core. The two panels are quite similar displaying smooth distribution of the velocities, implying that our procedure successfully inferred the line core Doppler shifts (in most of the pixels). In a small part of the FOV (for example, around [X, Y]=[8, 9.5] Mm), blue patches are discontinuously located in red-shifted regions. Such blue patches are not found in the middle panel, thus these correspond to bad fits from our method. The FOV, particularly at magnetic loops at the center, has the predominant downflows, as pointed out in some literatures (e.g., Leenaarts et al., 2013b).

In the right panel of Fig. 2.9, we show the joint probability density function (joint PDF) of the two above-mentioned velocities, showing a good correlation between them. The Pearson correlation of the velocities exceeds 80%. Note that we excluded the pixels having velocities larger than 20 km s^{-1} to eliminate the bad fits when we computed the
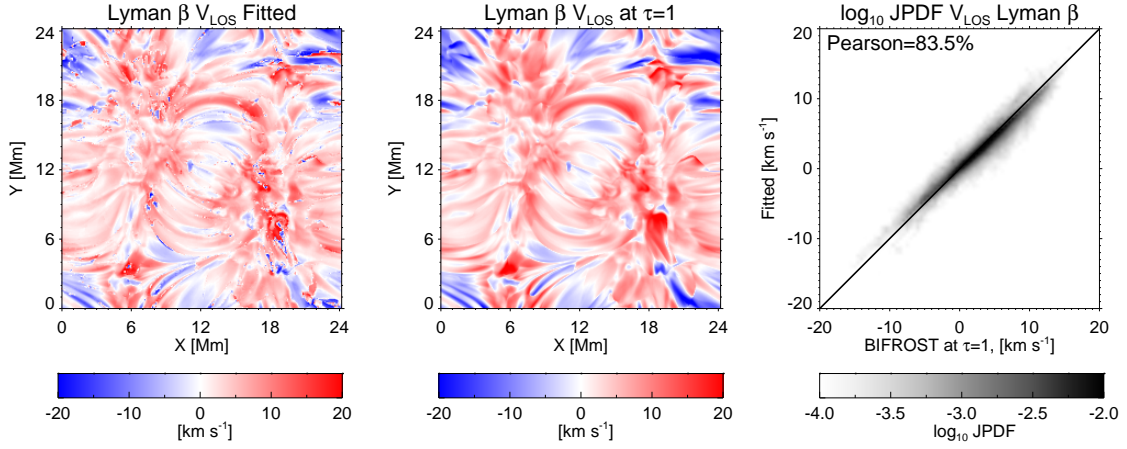
Figure 2.9: The LOS velocity derived from the line core Doppler shift of Lyβ (left). Middle panel shows the LOS velocity at the optical depth of Lyβ core is unity. A positive (negative) velocity corresponds to a downflow (upflow) represented with the red (blue) color codes, respectively. The joint PDF of the two types of velocities is shown in the rightmost panel. The Pearson correlation between them is displayed at the top-left of the panel. Black solid line represents y = x.

correlation. We can conclude that the Lyβ is an excellent diagnostic tool to probe the plasma dynamics at the upper chromosphere.

In addition, we examined the capabilities of the line core intensities as diagnostics of the electron density and the formation height. In the left panel of Fig. 2.10 we exhibit the joint PDF of the intensity and the squared electron density. The comparison proves their excellent correlation with the Pearson correlation of 85%. The correlation is probably because the Lyβ transition is dominated by collisions. This indicates that the core intensities are good tools to infer the local electron density at their formation heights. Strictly speaking, intensities have to be related with the product of the squared electron densities and the widths of the emitting region. We found that, from the RF to electron density at the core wavelength, the core intensity is sensitive to the perturbations of electron density in the region of 1 km width (FWHM). Since our 3D model atmosphere is vertically resolved with ~ 20 km pix^{-1}, it is difficult to discuss the effects of the widths. However, we expect that the effects of the widths changes each data point in the left panel of Fig. 2.10 by a few factor, then it does not significantly alter our results and the core intensity is sill a
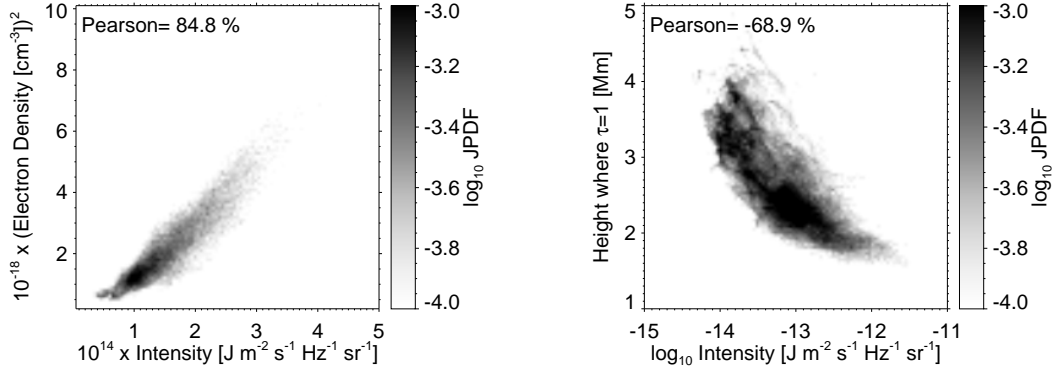
Figure 2.10: The joint PDFs of the squared electron density as a function of the intensity (left), and the height where $\tau = 1$ as a function of the logarithmic intensity (right), regarding the Lyβ core.

useful probe to the local electron densities, although the relationship is highly dependent on the atmospheric model. The joint PDF of the logarithmic emergent intensity and formation height is displayed in the right panel of Fig. 2.10. As shown in Fig. 2.8, these two parameters are anti-correlated to each other. The Pearson correlation is fairly good, i.e., 69%, although lower than the previous case. This means that the logarithmic intensity of the Lyβ line core displays the shape of the upper chromosphere with good accuracy.

2.4   Summary

In this chapter, we synthesized the Lyβ spectra, making use of the 1D semi-empirical atmosphere and 3D realistic MHD simulation by solving the radiative transfer and statistical equilibrium equations, and thoroughly examined their spectroscopic properties.

In the formation of Lyβ, NLTE populations and PRD effects in the Lyα and β transitions should be considered. The NLTE population of C only affects on the far wing of the Lyβ spectral profile. The core of Lyβ is sensitive to the temperature and LOS velocity perturbations at the upper chromosphere, and forms around 2.8 Mm above the solar surface where temperature is about 23,000 K. The line core Doppler shift is correlated with LOS velocity at the upper chromosphere very well. Its core intensity can be used as

diagnostics of the squared electron density and of the shape of the upper chromosphere.

If we focus on the entire profile of the Lyβ, this spectral line has the information of not only the upper chromosphere in the line core but also a wide range of chromospheric layers in its wing (see Fig. 2.7). The spectroscopic features of the wings and their implications for the physics in the chromosphere will be examined in the following chapters.

In conclusion, the Lyβ line core is excellent diagnostics to probe the plasma dynamics and thermal conditions in the solar middle atmosphere.

Chapter 3

Statistical Properties of Spectral Shapes

本章については 5 年以内に雑誌等で刊行予定のため非公開。

Chapter 4

Observed Lyβ Spectra

本章については 5 年以内に雑誌等で刊行予定のため非公開。

Chapter 5

Comparisons between Lyman α and β

本章については 5 年以内に雑誌等で刊行予定のため非公開。

Chapter 6

General Discussion

本章については 5 年以内に雑誌等で刊行予定のため非公開。

Chapter 7

Concluding Remarks

Our motivation in this dissertation is to characterize the Lyman transitions (Lyβ, in particular), which have the potential to probe the physics of the chromosphere at heights where we are not sensitive with standard traditional spectral lines found in the visible and UV spectral range. Since spectroscopic observations of Lyman lines are limited, we numerically computed Lyman spectra with the NLTE spectral line synthesis solving the full radiative transfer equations and characterized their responses to changes on the chromospheric plasma properties. Here, as concluding remarks, we answer the two questions determined in Sec. 1.4 and shortly summarize the future prospects.

To address the first issue, we quantified the capabilities of the line core, wing, and shape of the Lyβ spectra to diagnose the middle to upper chromosphere. Lyβ line core forms in the upper chromosphere of the temperature of $\sim 23{,}000$ K and responds well to the thermal conditions (i.e., geometrical structure and electron density) and gas dynamics (i.e., line-of-sight (LOS) velocity) at those layers (Chapter 2). Its wing has the capabilities to probe the temperature perturbation in 1.1-2.1 Mm and LOS velocity perturbations between 1.7-2.1 Mm in the semi-empirical FAL-C atmosphere. We also discovered that the emission peak asymmetry of Lyβ is a potential tool to diagnose the chromospheric dynamics since it correlates to the velocity gradient in the middle to upper chromosphere with high accuracy in Chapter 3. The cluster analysis allowed us to relate typical line

shapes of Lyβ to reference atmospheric stratifications and find a correlation between single-peak profiles and a narrow chromosphere shifted towards lower heights, and between multi-peak profiles and an upward-extended chromosphere. These synthetic analyses demonstrated that rich information is embedded in Lyβ spectra, e.g., LOS velocity, electron density, geometric structure of the upper chromosphere, and chromospheric velocity gradient. The comparison of the simulated spectra with that observed by SUMER in Chapter 4 showed that deeply reversed Lyβ spectra tend to be distributed on the top part of magnetic loops in both cases. We conclude that Lyβ core and wing are excellent tools to bridge the diagnostic gaps in the chromosphere to which we cannot access with modern spectroscopic facilities.

We further investigated the relationship between the opposite combination of the emission peak asymmetries in Lyα and β and the stratifications of LOS velocities in Chapter 5, which is the second goal we want to reach. The opposite combination reported in previous works, i.e., blue asymmetric Lyα and red asymmetric Lyβ, can be reproduced by a red-shift at the core and a negative velocity gradient that extends lower than 2 Mm, in the modified FAL-C atmosphere. We suggest these emission peak asymmetries are new useful tools when we accurately estimate the velocity stratification in the chromosphere which is related to the heating mechanism in the background.

Chromospheric diagnostics by the Lyman lines will be excellent tools to understand the role of the middle to upper chromosphere on the atmospheric heating if their observations are achieved in future. The intense emission of the Lyman lines is suitable to conduct high cadence spectroscopic observations, which allow us to identify the modes of high-frequency waves and to estimate their energy budget, whose impact on the atmospheric heating is still under debate. Simultaneous observations with other chromospheric lines (e.g., Ca II H&K and Mg II h&k) will make seamless estimations of energy transportation and dissipation possible. Moreover, the formation mechanism of spicules will be distinguished by probing their acceleration with the asymmetry of Lyβ, which help us understand their role in the coronal heating. The observations mentioned above might be

conducted through spectroscopic observations in the 2020's by the space-born EUVST from the earth orbit and SolO/SPICE out of the ecliptic plane.

References

Anderson, L. S., & Athay, R. G. 1989a, The Astrophysical Journal, 336, 1089

—. 1989b, The Astrophysical Journal, 346, 1010

Asplund, M., Grevesse, N., Sauval, A. J., & Scott, P. 2009, Annual Review of Astronomy and Astrophysics, 47, 481

Asplund, M., Nordlund, Å., Trampedach, R., Allende Prieto, C., & Stein, R. F. 2000, Astronomy & Astrophysics, 359, 729

Athay, R. G. 1976, The solar chromosphere and corona: Quiet sun, Vol. 53

Beckers, J. M. 1968, Solar Physics, 3, 367

—. 1972, Annual Review of Astronomy and Astrophysics, 10, 73

Bjørgen, J. P., Sukhorukov, A. V., Leenaarts, J., Carlsson, M., de la Cruz Rodríguez, J., Scharmer, G. B., & Hansteen, V. H. 2018, Astronomy & Astrophysics, 611, A62

Cally, P. S., & Goossens, M. 2008, Solar Physics, 251, 251

Carlsson, M. 1986, Uppsala Astronomical Observatory Reports, 33

Carlsson, M., De Pontieu, B., & Hansteen, V. H. 2019, Annual Review of Astronomy and Astrophysics, 57, 189

Carlsson, M., Hansteen, V. H., Gudiksen, B. V., Leenaarts, J., & De Pontieu, B. 2016, Astronomy & Astrophysics, 585, A4

Carlsson, M., & Stein, R. F. 1997, The Astrophysical Journal, 481, 500

Cranmer, S. R. 2009, Living Reviews in Solar Physics, 6, 3

Curdt, W., Tian, H., Teriaca, L., Schühle, U., & Lemaire, P. 2008, Astronomy & Astrophysics, 492, L9

Dadashi, N., Teriaca, L., & Solanki, S. K. 2011, Astronomy & Astrophysics, 534, A90

De Pontieu, B., McIntosh, S. W., Hansteen, V. H., & Schrijver, C. J. 2009, The Astrophysical Journal Letters, 701, L1

De Pontieu, B., et al. 2007a, Publications of Astronomical Society of Japan, 59, S655

—. 2007b, Science, 318, 1574

—. 2011, Science, 331, 55

—. 2014, Solar Physics, 289, 2733

Del Zanna, G., & Mason, H. E. 2018, Living Reviews in Solar Physics, 15, 5

Dere, K. P., Landi, E., Mason, H. E., Monsignori Fossi, B. C., & Young, P. R. 1997, Astronomy & Astrophysics Supplement Series, 125, 149

Domingo, V., Fleck, B., & Poland, A. I. 1995, Solar Physics, 162, 1

Doschek, G. A., Feldman, U., & Bohlin, J. D. 1976, The Astrophysical Journal Letters, 205, L177

Fontenla, J. M., Avrett, E. H., & Loeser, R. 1990, The Astrophysical Journal, 355, 700

—. 1991, The Astrophysical Journal, 377, 712

—. 1993, The Astrophysical Journal, 406, 319

Gary, G. A. 2001, Solar Physics, 203, 71

Grant, S. D. T., et al. 2018, Nature Physics, 14, 480

Gudiksen, B. V., Carlsson, M., Hansteen, V. H., Hayek, W., Leenaarts, J., & Martínez-Sykora, J. 2011, Astronomy & Astrophysics, 531, A154

Gunár, S., Heinzel, P., Anzer, U., & Schmieder, B. 2008, Astronomy & Astrophysics, 490, 307

Gunár, S., Heinzel, P., Schmieder, B., Schwartz, P., & Anzer, U. 2007, Astronomy & Astrophysics, 472, 929

Hannah, I. G., Hudson, H. S., Battaglia, M., Christe, S., Kašparová, J., Krucker, S., Kundu, M. R., & Veronig, A. 2011, Space Science Reviews, 159, 263

Hansteen, V. H., De Pontieu, B., Rouppe van der Voort, L., van Noort, M., & Carlsson, M. 2006, The Astrophysical Journal Letters, 647, L73

Hansteen, V. H., Hara, H., De Pontieu, B., & Carlsson, M. 2010, The Astrophysical Journal, 718, 1070

Hara, H., Watanabe, T., Harra, L. K., Culhane, J. L., Young, P. R., Mariska, J. T., & Doschek, G. A. 2008, The Astrophysical Journal Letters, 678, L67

Hasegawa, T., Noda, C. Q., Shimizu, T., & Carlsson, M. 2020, The Astrophysical Journal, 900, 34

Heinzel, P., & Anzer, U. 2001, Astronomy & Astrophysics, 375, 1082

Heinzel, P., Anzer, U., & Gunár, S. 2005, Astronomy & Astrophysics, 442, 331

Heinzel, P., Schmieder, B., Vial, J. C., & Kotrč, P. 2001, Astronomy & Astrophysics, 370, 281

Heyvaerts, J., & Priest, E. R. 1983, Astronomy & Astrophysics, 117, 220

Ionson, J. A. 1978, The Astrophysical Journal, 226, 650

Ishikawa, R., et al. 2017, The Astrophysical Journal, 841, 31

Kano, R., et al. 2017, The Astrophysical Journal Letters, 839, L10

Klimchuk, J. A. 2006, Solar Physics, 234, 41

Kohutova, P., Verwichte, E., & Froment, C. 2020, Astronomy & Astrophysics, 633, L6

Kubo, M., et al. 2016, The Astrophysical Journal, 832, 141

Landi Degl'Innocenti, E., & Landi Degl'Innocenti, M. 1977, Astronomy & Astrophysics, 56, 111

Langangen, Ø., De Pontieu, B., Carlsson, M., Hansteen, V. H., Cauzzi, G., & Reardon, K. 2008, The Astrophysical Journal Letters, 679, L167

Leenaarts, J., & Carlsson, M. 2009, Astronomical Society of the Pacific Conference Series, Vol. 415, MULTI3D: A Domain-Decomposed 3D Radiative Transfer Code, ed. B. Lites, M. Cheung, T. Magara, J. Mariska, & K. Reeves, 87

Leenaarts, J., Carlsson, M., & Rouppe van der Voort, L. 2012, The Astrophysical Journal, 749, 136

—. 2015, The Astrophysical Journal, 802, 136

Leenaarts, J., Pereira, T. M. D., Carlsson, M., Uitenbroek, H., & De Pontieu, B. 2013a, The Astrophysical Journal, 772, 89

—. 2013b, The Astrophysical Journal, 772, 90

Lemaire, P., Charra, J., Jouchoux, A., Vidal-Madjar, A., Artzner, G. E., Vial, J. C., Bonnet, R. M., & Skumanich, A. 1978, The Astrophysical Journal Letters, 223, L55

Lemaire, P., et al. 1997, Solar Physics, 170, 105

Lin, H.-H., & Carlsson, M. 2015, The Astrophysical Journal, 813, 34

Madjarska, M. S. 2019, Living Reviews in Solar Physics, 16, 2

McIntosh, S. W., & De Pontieu, B. 2009, The Astrophysical Journal, 707, 524

McIntosh, S. W., de Pontieu, B., Carlsson, M., Hansteen, V., Boerner, P., & Goossens, M. 2011, Nature, 475, 477

McIntosh, S. W., Tian, H., Sechler, M., & De Pontieu, B. 2012, The Astrophysical Journal, 749, 60

Okamoto, T. J., et al. 2007, Science, 318, 1577

Parker, E. N. 1972, The Astrophysical Journal, 174, 499

—. 1983, The Astrophysical Journal, 264, 642

—. 1988, The Astrophysical Journal, 330, 474

Peter, H., & Judge, P. G. 1999, The Astrophysical Journal, 522, 1148

Pneuman, G. W., & Kopp, R. A. 1978, Solar Physics, 57, 49

Priest, E. 2014, Magnetohydrodynamics of the Sun

Quintero Noda, C., Shimizu, T., de la Cruz Rodríguez, J., Katsukawa, Y., Ichimoto, K., Anan, T., & Suematsu, Y. 2016, Monthly Notices of the Royal Astronomical Society, 459, 3363

Rathore, B., Carlsson, M., Leenaarts, J., & De Pontieu, B. 2015, The Astrophysical Journal, 811, 81

Reale, F. 2014, Living Reviews in Solar Physics, 11, 4

Reeves, E. M. 1976, Solar Physics, 46, 53

Rouppe van der Voort, L., Leenaarts, J., de Pontieu, B., Carlsson, M., & Vissers, G. 2009, The Astrophysical Journal, 705, 272

Rybicki, G. B., & Hummer, D. G. 1992, Astronomy & Astrophysics, 262, 209

Rybicki, G. B., & Lightman, A. P. 1986, Radiative Processes in Astrophysics

Samanta, T., et al. 2019, Science, 366, 890

Scharmer, G. B., Bjelksjo, K., Korhonen, T. K., Lindberg, B., & Petterson, B. 2003, in Society of Photo-Optical Instrumentation Engineers (SPIE) Conference Series, Vol. 4853, Proc. SPIE, ed. S. L. Keil & S. V. Avakyan, 341–350

Scharmer, G. B., et al. 2008, The Astrophysical Journal Letters, 689, L69

Schmit, D., et al. 2017, The Astrophysical Journal, 847, 141

Shibata, K., & Magara, T. 2011, Living Reviews in Solar Physics, 8, 6

Shimizu, T. 1995, Publications of Astronomical Society of Japan, 47, 251

Štěpán, J., & Trujillo Bueno, J. 2016, The Astrophysical Journal Letters, 826, L10

Sturrock, P. A., Roald, C. B., & Wolfson, R. 1999, The Astrophysical Journal Letters, 524, L75

Sukhorukov, A. V., & Leenaarts, J. 2017, Astronomy & Astrophysics, 597, A46

Teriaca, L., Banerjee, D., & Doyle, J. G. 1999, Astronomy & Astrophysics, 349, 636

Tian, H., Curdt, W., Marsch, E., & Schühle, U. 2009a, Astronomy & Astrophysics, 504, 239

Tian, H., Teriaca, L., Curdt, W., & Vial, J.-C. 2009b, The Astrophysical Journal Letters, 703, L152

Trujillo Bueno, J., et al. 2018, The Astrophysical Journal Letters, 866, L15

Uitenbroek, H. 2001, The Astrophysical Journal, 557, 389

Uitenbroek, H. 2006, in Astronomical Society of the Pacific Conference Series, Vol. 354, Solar MHD Theory and Observations: A High Spatial Resolution Perspective, ed. J. Leibacher, R. F. Stein, & H. Uitenbroek, 313

Van Doorsselaere, T., Gijsen, S. E., Andries, J., & Verth, G. 2014, The Astrophysical Journal, 795, 18

Vernazza, J. E., Avrett, E. H., & Loeser, R. 1981, The Astrophysical Journal Supplement Series, 45, 635

Vial, J. C., Ebadi, H., & Ajabshirizadeh, A. 2007, Solar Physics, 246, 327

Warren, H. P., Mariska, J. T., & Wilhelm, K. 1998, The Astrophysical Journal Supplement Series, 119, 105

Wedemeyer-Böhm, S., Lagg, A., & Nordlund, Å. 2009, Space Science Reviews, 144, 317

Wilhelm, K., et al. 1995, Solar Physics, 162, 189

Withbroe, G. L., & Noyes, R. W. 1977, Annual Review of Astronomy and Astrophysics, 15, 363

Xia, L. D., Marsch, E., & Wilhelm, K. 2004, Astronomy & Astrophysics, 424, 1025

Yoshida, M., et al. 2019, The Astrophysical Journal, 887, 2

Zhang, M., Xia, L. D., Tian, H., & Chen, Y. 2010, Astronomy & Astrophysics, 520, A37

Zirker, J. B. 1977, in Coronal Holes and High Speed Wind Streams, ed. J. B. Zirker, 1–26